

Review

A Review of the Structural Design of Anode Materials in Sodium-Ion Batteries Based on MXenes and Their Composites

Mengwei Yuan ^{1,*†}, Xingzi Zheng ^{2,†}, Jingshen Xu ², Qiao Ni ¹ , Luoqi Luo ¹, Zejun Cai ¹, Zemin Sun ¹, Liu Lin ¹ and Genban Sun ^{1,2,*}

¹ Center for Advanced Materials Research, Beijing Normal University, Zhuhai 519087, China

² College of Chemistry, Beijing Normal University, Beijing 100875, China

* Correspondence: mwyuan@mail.bnu.edu.cn (M.Y.); gbsun@bnu.edu.cn (G.S.)

† These authors contributed equally to this work.

Abstract: The typical two-dimensional layered structure materials, MXenes, are widely used in energy conversion and storage due to their high conductivity, ion transport ability, and rich surface structures. Recently, MXenes and their composites have been widely employed in secondary batteries, especially sodium-ion batteries (SIBs), with obvious performance improvement. As anodic materials, MXenes, metal oxides, metal sulfides, and other materials contain certain advantages in Na⁺ storage, but they individually also suffer from some issues and challenges, such as low conductivity and serious volume change, as well as the associated low capacity and poor cyclability. By virtue of the advantages of MXenes, with their high conductivity and ultrathin two-dimensional structures, the construction of surface-functionalized MXenes and MXene-based composites could effectively improve the conductivity and mass-transport properties of composites, alleviate volume expansion, and, thus, enhance the capacity properties, rate performances, and cycle stability of SIBs. Herein, we review the latest research status of the structural design of MXenes and MXene-based materials, as well as their applications in SIBs. We briefly introduce the research background and introduce MXenes and SIBs, and focus on their structural designs and corresponding applications in SIBs. Finally, the important challenges of MXene-based materials applied to SIBs are discussed, and the future prospects of MXene-based composite developments in SIBs are presented.

Keywords: Na-ion battery; two-dimensional structure; MXene-based materials; energy storage device; structure design



Citation: Yuan, M.; Zheng, X.; Xu, J.; Ni, Q.; Luo, L.; Cai, Z.; Sun, Z.; Lin, L.; Sun, G. A Review of the Structural Design of Anode Materials in Sodium-Ion Batteries Based on MXenes and Their Composites. *Batteries* **2023**, *9*, 48. <https://doi.org/10.3390/batteries9010048>

Academic Editor: Claudio Gerbaldi

Received: 30 November 2022

Revised: 25 December 2022

Accepted: 4 January 2023

Published: 8 January 2023



Copyright: © 2023 by the authors. Licensee MDPI, Basel, Switzerland. This article is an open access article distributed under the terms and conditions of the Creative Commons Attribution (CC BY) license (<https://creativecommons.org/licenses/by/4.0/>).

1. Introduction

The utilization of renewable energy is significant in achieving sustainable energy supplies. In particular, the use of clean energy, including wind, water, solar, and tidal energy, as well as other renewable energy sources, could effectively relieve carbon emissions and become a promising alternative for the future power industry [1,2]. However, the instability and discontinuity of renewable energy, which is significantly affected by environment and climate conditions, requires highly efficient energy conversion and storage devices (ECSDs). Electrochemical ECSDs, such as secondary batteries, supercapacitors, and fuel cells, have been widely used in recent decades [3–8]. Among them, rechargeable secondary batteries are the most effective electrochemical ECSD technologies, especially Li-ion batteries (LIBs), which are endowed with high energy density, long life cycles, environmental friendliness, and low self-discharge rates [9,10]. As a typical electrochemical ECSD, LIBs are used in electric vehicles, portable electronic devices, wearable energy devices, large-scale energy storage, and other fields [5,11,12]. However, the Li content in the Earth's crust is only 0.0065%, and the need for lithium resources has also increased significantly with the large-scale use of LIBs, which has meant that it has gradually failed to meet the growing demand [2]. These reasons have further aggravated the rise in the cost of LIBs, making

them gradually lose their advantages in low-speed electric vehicles, large-scale energy storage, and portable electronic devices.

Na and Li belong to the IA group, which is endowed with similar chemical and physical properties. In the crust, the Na content is 2.75%, more than 400 times that of Li, and it is rich and has a low cost [2]. Thus, SIBs with similar rocking-chair mechanisms based on Na⁺ reactions have attracted more attention [13]. In aprotic systems, the Na⁺/Na electrode potential is -2.93 V, close to that of Li⁺/Li (-3.05 V), which is conducive to improving battery voltage and energy density [14–16]. In addition, the desolvation energy of Na⁺ based on propylene carbonate solvent is 158.2 kJ/mol, obviously lower than that of Li⁺ (215.8 kJ/mol), which can form small solvated ions with faster diffusion kinetics in the battery reaction [17]. More importantly, the similar properties of Li and Na mean that the research and development of SIBs have many reference bases. For example, substituting many Li-containing cathodic materials with electrochemical activity with Na would lead to similar activity in SIBs, such as NaFePO₄, NaCo_{1-x-y}Ni_xMn_yO₂, and other layered rock-salt structures [18]. The transition metal oxides, sulfides, and carbon materials, as well as silicon, have superior Li⁺ storage performance and also cause electrochemical activity in SIBs. This similar technical route has helped researchers make important progress in the research and development of SIBs, and the technologies have developed rapidly in a relatively short time [1,18–23]. However, large differences in the radius of movable ions (1.02 and 0.76 Å for Na⁺ and Li⁺) result in slow kinetics, serious volume expansion in discharge–charge processes, and capacity decay, as well as the poor rate performance and cyclability of SIBs. Thus, it is the main bottleneck in developing long-life electrode materials with the stable intercalation/deintercalation of Na⁺, which seriously restricts the practical application of SIBs in the future [19].

MXenes are novel two-dimensional (2D) materials with excellent conductivity and low ion diffusion barriers that are widely used in energy storage and conversion, electrolysis, adsorption, and other surface-related fields [24–27]. MXenes, such as Ti₃C₂, are fabricated by selectively etching Al layers in MAX Ti₃AlC₂ and have become one of the most important materials in electrochemical ESCDs. MXenes can mainly be obtained using two typical etching methods: wet chemical etching and molten salt etching. The resultant ultrathin 2D MXenes have large specific surface areas, high conductivity, rich active sites, and 2D ion transport channels [28], which can provide rich active sites for ion storage and enhanced reaction kinetics [27,28]. These superior properties endow them with highly applicable potential in SIBs, LIBs, Li-O₂ batteries, Li-S batteries, aqueous Zn-ion batteries, and supercapacitors [29–34]. As electrode materials, their ultrathin structures have large specific areas, which are conducive to mass transport in the electrode, especially regarding the accessibility of electrolytes [35,36]. Simultaneously, with a typical layered structure, they have large layer spacing, which benefits the transfer of large ions in the interlayer and presents unobvious volume changes, ensuring structural stability. In addition, surface areas with functionalized group terminations could serve as active sites to adsorb or capture intermediators in discharge–charge processes. More importantly, this 2D structure has excellent electron conductivity, which causes fast electron transfer in the discharge–charge process and facilitates reaction kinetics [31,37]. In addition, MXenes have good adjustability, which can be converted from an accordion-like three-dimensional (3D) structure into nanodots, nanobelts, nanosheets, and porous 3D structures. They can also be functionalized using controllable surface modification via loading or the in situ generation strategy to construct new and highly efficient composites.

For MXenes, when used in batteries as active materials, their performance is limited by inevitable stacking, resulting in low capacity as well as poor durability and rate performances [26,38]. To effectively utilize MXenes, there has been extensive research carried out to optimize their electrochemical performance via surface structure functional modification, as well as the construction of heterostructures and hybrid structures. When MXenes are employed in compounding, their layered structures could provide more channels, and other materials adhering to MXenes or grown between MXene sheets could expand the

layered space in MXenes and relieve the volume expansion in operation. Therefore, MXenes have good advantages in enhancing the stability and reversibility of sodium storage, and they can be developed into materials with high-capacity and good rate performance via reasonable structural design and combining their advantages with other sodium storage materials. There have been many reviews on the composites and applications of MXenes and MXene-based materials; however, the structural design of MXene-based materials and their applications in the anodic materials of SIBs are less reviewed. With the commercialization of SIBs, their key technical indicators, such as their capacity properties and rate performance, need to be further improved, which is a huge challenge. Therefore, this paper selected promising MXene-based electrode materials as the research objects and summarizes the research on the anodes of SIBs in recent years, hoping to provide some new ideas on the development of new electrode materials from the perspective of structural design.

2. Structure and Synthesis of MXenes

2.1. Structure Characteristics

MXenes contain transition metal carbides and nitrides, marked as $M_{n+1}X_nT_x$. MXenes are obtained by etching MAX ($M_{n+1}AX_n$), as shown in Figure 1a, where M is the Ti, Mo, Zr, and Cr elements; A is the Al, Si, Ga, and Ge elements; X is the C and N elements; and T is the functional groups on the MXene's surface [39]. MXenes have a hexagonal, closely packed structure with an ABABAB type. However, due to the influence of element proportions, face-centered cubic structures also exist in $M_{3 \times 2}$ and M_4X_3 with an ABCABC type [40]. Many MXene types have been explored and reported over the past decade, such as Ti_2C , Ti_3C_2 , Ti_3CN , Ti_4N_3 , V_2C , Cr_3TiC_2 , Mo_2C , Mo_3ScC_2 , Zr_3C_2 , and Nb_2C [39–42]. The structure of MXenes is highly dependent on the parent materials. Among these different MXenes, Ti_3C_2 has been widely investigated due to its accessibility, which is obtained from the hexagonal structure of Ti_3AlC_2 , even with scale-up production [43]. With the removal of the Al layer from Ti_3AlC_2 , the Ti_3C_2 phase presents high electron density at the Fermi level compared with the parent-phase Ti_3AlC_2 , displaying metal conductivity. For MXenes, the majority of them have metal-like electron conductivity and hydrophilic natures due to conductive cores and rich surface-functionalized groups formed in the preparation process, which have good adjustability [44]. Benefitting from their unique structure, MXenes are considered promising 2D materials in electrochemical energy conversion and storage.

2.2. Controllable Synthesis

MXenes are usually prepared by selectively removing A from the $M_{n+1}AX_n$ phase with Lewis acid (an HF solution, a mixing fluoride solution, or molten salt-containing halogen ions, as shown in Figure 1b) [27]. After etching, an MXene changes from the block structure of its precursor to an accordion-like structure, and the surface of the MXene sheet will produce rich functional groups, such as F and OH, which also lay a structural foundation for the MXene's easily modified properties. To obtain high-quality MXenes, the accordion-like structure needs to be further intercalated and stripped to form ultrathin MXene nanosheets so as to assure the advantages of having large surface areas and high conductivity. In an HF solution system, after etching, the MXene is chemically intercalated with organic molecules (such as DMSO and TMAOH) to form monolayer or few-layer MXene nanosheets [45]. As for the mixing fluoride solution method (HCl + LiF/NaF/KF), which is a more environmentally friendly and safer strategy, the combination of HCl and fluoride salts generates the HF solution and intercalation solvent, so the etching and delamination processes can be carried out simultaneously, which is for better controlling the MXene's size and quality [46]. MXenes can also be obtained in molten salt, avoiding oxidation and surface defects, as well as producing adjustable functional groups. For example, $Ti_3C_2Br_2$ was successfully synthesized by halogen-compound-etching Ti_3AlC_2 in [47], while iodine in anhydrous acetonitrile benefited to oxygen-terminal Ti_3C_2Tx [48]. In addition, Sun et al. successfully realized MXenes exfoliated under fluoride-free action

with LIB reactions by al-loying Li and Al layers at low potential, combined with the strategy of using a water-phase micro-explosion reaction, which is a relatively new and environmentally friendly method but may be limited by the output of products [49]. At present, this method is not widely used. Even so, the synthesis method, which used etchant, pH conditions, and treated temperatures, could affect the quality and productivity of MXenes, as well as the determination of the termination type and its distribution [44]. Therefore, in order to obtain an MXene with a specific structure and composition, it is very important to select appropriate preparation methods and conditions, which play an important role in the subsequent functionalization or further applications of MXenes. As new, ultrathin 2D materials, MXenes have many advantages and excellent characteristics, such as adjustable layer spacing, high conductivity, outstanding mechanical stability, rich polar functional groups, large surface areas, and modifiability. Therefore, they are widely used in electrochemical energy storage, such as SIBs, LIBs, Li-S batteries, Li-O₂ batteries, and supercapacitors [31,32,34,49,50].

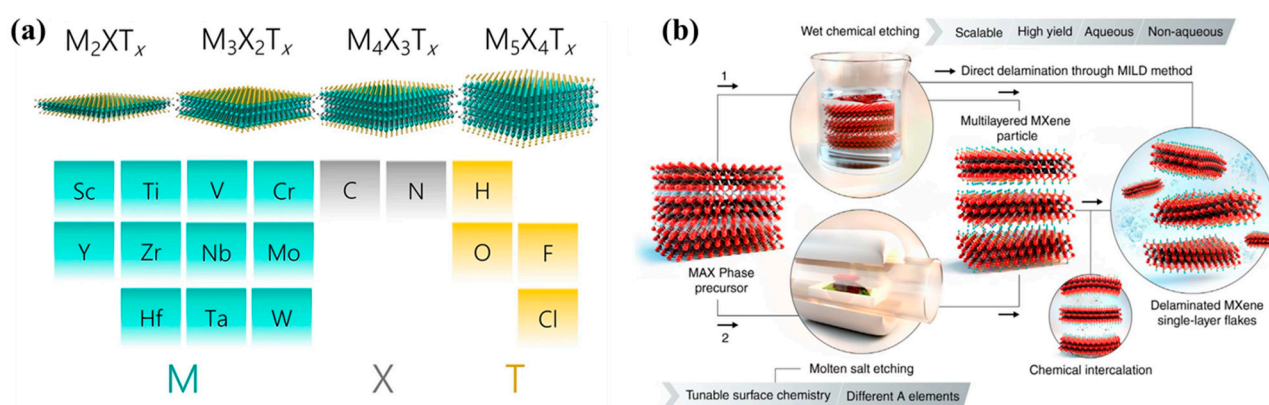


Figure 1. (a) Illustration of the structural categories of 2D MXenes (reproduced with permission from Ref. [51]; copyright 2021, Springer). (b) Schematics of the main strategies for producing MXenes by removing A layers from MAX via F-containing acids and molten salt etching (reproduced with permission from Ref. [27]; copyright 2021, *Science*).

3. Anode Materials Based on MXenes and Their Composites

Sodium storage performance based on MXenes is restricted by inevitable stacking, low specific capacity, and high charge voltage [25,26,52]. To effectively utilize MXenes, many studies have been carried out. One of the main strategies is to effectively regulate the composition, structure, and surface characteristics of MXenes in order to achieve excellent sodium storage activities. Another important strategy is to construct MXene-based composite structures [1]. In composites, layered MXenes can provide more ion channels, and other sodium storage materials uniformly adhered to or grown on MXene sheets can expand the layered space. In particular, cheap, nonmetal materials such as Si, P, C, and low-cost oxides and sulfides have relatively high theoretical capacities [52–55]. However, as shown in Figure 2, most of them result in low electron conductivity and serious volume expansion in discharge–charge processes, which results in poor rate performances and cyclability. As we know, reducing the particle size and simultaneously introducing a high-conductivity substrate are effective ways of improving performance. Thus, the construction of MXene-based composites with sodium storage materials could improve specific capacity, cyclability, and rate performance via enhanced conductivity, stable intercalation/deintercalation, and promoted kinetics, which is the current focus of research. Herein, we review the current research progress, especially the structural design and applications in SIBs from the perspective of MXenes and their related composites, including nonmetal materials/MXenes, metal-oxides/MXenes, sulfides/MXenes, and other MXene-based composites (Figure 2). All of the performance structures of these materials are summarized.

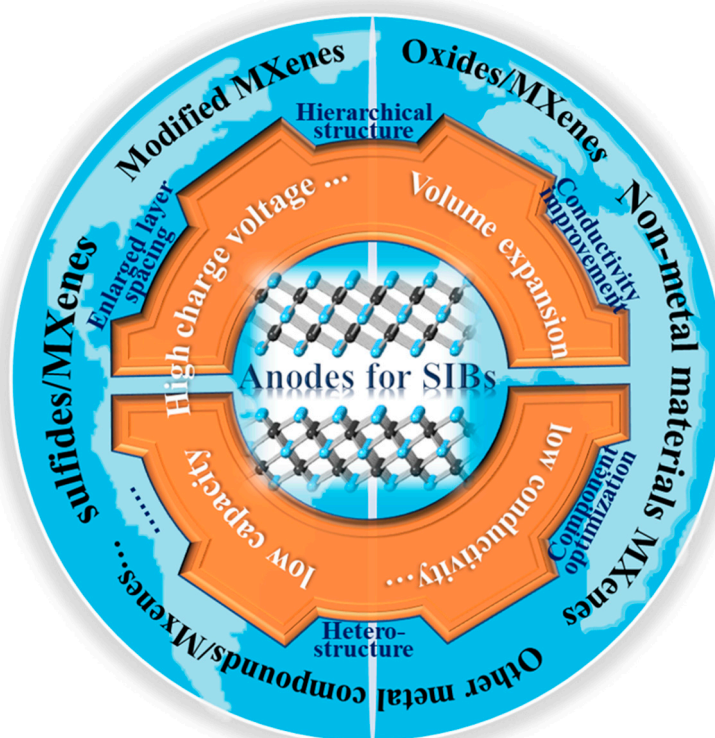


Figure 2. Problems in SIBs and the structural designs of MXene-based materials.

3.1. Anode Materials Based on Pure MXenes

The low ionic/electron transfer kinetics in electrodes is one of the limiting factors in developing high-performance anode materials. There are many useful structures employed to improve the battery performance, and the key parameters are listed in Table 1, which presents the obvious improvements. In detail, Yang et al. investigated the application of different MXenes in SIBs via density functional theory (DFT), inferring the weak interaction between Na^+ and MXenes [56]. The lower diffusion activation energy in MXenes may be beneficial to ion migration, leading to fast Na^+ transmission and making them promising anode materials. Lv et al. prepared $\text{Ti}_3\text{C}_2\text{T}_x$ with HF etching and associated with sonication in DMSO, which presented a specific capacity of 110 mAh/g at 0.1 A/g [57]. The DMSO intercalating into the $\text{Ti}_3\text{C}_2\text{T}_x$ improved the specific area by enlarging the spacing, thus obtaining a few-layer structure, which effectively facilitated the electrode reaction and led to obvious performance improvement. Liang et al. reported that $\text{Ti}_2\text{C}_{0.5}\text{N}_{0.5}\text{T}_x$ spontaneously intercalated by tetramethylammonium—which was treated by sonication in water—had the potential to produce 2D nanosheets on a large scale [58]. $\text{Ti}_2\text{C}_{0.5}\text{N}_{0.5}\text{T}_x$ showed a capacity of 182 mAh/g at 0.02 A/g with a coulombic efficiency (CE) of 70%, higher than that of Ti_2CT_x due to the introduction of N with more efficient electroactive sites.

Table 1. Performance comparison of different MXene anodes in SIBs.

Materials	Long-Term Capacity	Current Density	Cycle Number	Rate Performance	Charge Voltage at Medium Capacity	Ref.
$\text{Ti}_3\text{C}_2\text{T}_x$	103 mAh/g	0.1 A/g	500	85 mAh/g@0.5 A/g	~1.5 V	[57]
$\text{Ti}_2\text{C}_{0.5}\text{N}_{0.5}\text{T}_x$	46 mAh/g	0.2 A/g	500	60 mAh/g@1 A/g	~1.5 V	[58]
Nb_2CT_x	102 mAh/g	1 A/g	500	99 mAh/g@2 A/g	~1.7 V	[59]
3D $\text{Ti}_3\text{C}_2\text{T}_x$	295 mAh/g	2.5 C	1000	120 mAh/g@25 C	~1.5 V	[60]
3D V_2CT_x	310 mAh/g	2.5 C	1000	170 mAh/g@25 C	~1.5 V	[60]
3D Mo_2CT_x	290 mAh/g	2.5 C	1000	125 mAh/g@25 C	~1.5 V	[60]

Table 1. Cont.

Materials	Long-Term Capacity	Current Density	Cycle Number	Rate Performance	Charge Voltage at Medium Capacity	Ref.
Porous $\text{Ti}_3\text{C}_2\text{T}_x$	189 mAh/g	1 A/g	1000	24 mAh/g@100 A/g	~1.75 V	[37]
P- $\text{Ti}_3\text{C}_2\text{T}_x$	68 mAh/g	0.5 A/g	500	88 mAh/g@5 A/g	~1.6 V	[61]
a- Ti_3C_2 MNRs	~50 mAh/g	0.2 A/g	500	83 mAh/g@0.3 A/g	~1.0 V	[62]
Oligolayered $\text{Ti}_3\text{C}_2\text{T}_x$	280 mAh/g	0.5 A/g	500	340 mAh/g@1 A/g	~1.5 V	[63]
Na-c- $\text{Ti}_3\text{C}_2\text{T}_x$	54 mAh/g	1.5 A/g	1000	61 mAh/g@1 A/g	~1.75	[64]
Na- Ti_3C_2	85 mAh/g	2 A/g	2000	~110 mAh/g@3 A/g	~1.3 V	[65]
S- $\text{Ti}_3\text{C}_2\text{T}_x$	74.2 mAh/g	0.5 A/g	2000	113.9 mAh/g@4 A/g	~1.5 V	[66]
S- Ti_3C_2	135 mAh/g	2 A/g	1000	136.6 mAh/g@5 A/g	~1.5 V	[67]

The serious stacking of two-dimensional materials largely restricts their applications in ECSDs. In order to make full use of MXene materials and their electrochemical energy storage properties, Zhao et al. constructed a series of self-supporting 3D macroporous MXene frameworks with hollow MXene spheres (Figure 3a,b) using the PMMA template method, and they presented good hydrophobicity with a large water contact angle compared with the compact one in Figure 3c,d [60]. As expected, the as-prepared 3D $\text{Ti}_3\text{C}_2\text{T}_x$, V_2CT_x , and Mo_2CT_x electrodes presented specific capacities of ~330, 340, and 370 mAh/g, with CEs of 53.8%, 55.3%, and 51.2%, which then demonstrated ~300 mAh/g after 1000 cycles at 2.5 C (Figure 3e), showing a superior rate performance. Xie et al. prepared highly conductive $\text{Ti}_3\text{C}_2\text{T}_x$ nanosheets formed with a porous structure and a high specific area using a novel S template method (Figure 3f,g), which was conducive to enhancing the Na^+ storage kinetics [37]. The porous $\text{Ti}_3\text{C}_2\text{T}_x$ electrode delivered 166, 124, and 24 mAh/g at 1, 10, and 100 A/g. Its electrode also exhibited 1000 cycles at 1 A/g without obvious capacity decay. Natu et al. reported a mesoporous $\text{Ti}_3\text{C}_2\text{T}_x$ structure. This benefited from a mesoporous architecture with superior conductivity and accessibility; a capacity of 120 mAh/g (0.5 A/g) was achieved [68]. Ming et al. showed a porous $\text{Ti}_3\text{C}_2\text{T}_x$ texture (P- $\text{Ti}_3\text{C}_2\text{T}_x$) with a 3D architecture that delivered 140 mAh/g after 150 cycles in which the defects and vacancies provided the extra electroactive sites, and it was dominated by the capacitive contribution [61].

To further optimize the surface area and interlayer spacing, Lian et al. prepared alkalinized Ti_3C_2 nanoribbons (a- Ti_3C_2 MNRs) using the continuous shaking treatment on pristine Ti_3C_2 in a KOH solution—as shown in Figure 3i—and these ribbons had a 3D porous structure with expanded interlayer spacing and narrow widths [62]. This unique structure was endowed with strong stability and could promote ion reaction kinetics, which illustrated the SIB performance, delivering ~50 mAh/g after 500 cycles. Song et al. reported on oligolayered $\text{Ti}_3\text{C}_2\text{T}_x$ with a capacity of 280 mAh/g at 0.5 A/g after 500 cycles [63]. This electrochemical study suggested that the surface-controlled redox reaction was the main charge storage type for the oligolayered $\text{Ti}_3\text{C}_2\text{T}_x$. This impressive performance demonstrated the highlights of this architecture and even broadened its applications.

A similar result for porous structures was achieved by Zhao et al., who illustrated a Na^+ -induced, crumpling, porous $\text{Ti}_3\text{C}_2\text{T}_x$ electrode (Na-c- $\text{Ti}_3\text{C}_2\text{T}_x$) that also showed high reversible capacity and cyclability [64]. An analogous strategy with alkali-metal-ion-pillared Ti_3C_2 was also prepared with Na^+ by Luo et al., presenting facilitated kinetics due to increased interlayer spacing (Figure 3j) and a decrease in the Na^+ diffusion barrier, showing the excellent cyclability of 2000 cycles at 2 A/g [65]. Li et al. [66] employed the S-doped strategy via a facile sulfidation treatment to improve the conductivity and expand the interlayer of $\text{Ti}_3\text{C}_2\text{T}_x$. The S-doped $\text{Ti}_3\text{C}_2\text{T}_x$ (S- $\text{Ti}_3\text{C}_2\text{T}_x$) exhibited 183.2 mAh/g with a CE of 63%, and it presented a superior rate performance of 113.9 mAh/g at 4 A/g, as well as durability after 2000 cycles. On this basis, Sun et al. combined the strategy of Na^+ pillaring and sulfur doping to construct a new structure (S- Ti_3C_2) with 135 mAh/g and 1000 cycles of durability, which benefitted from an enlarged interlayer and a quick Na^+ transport path [67]. Even so, this unique structure had a coulombic efficiency of 58.6%, which needed further optimization.

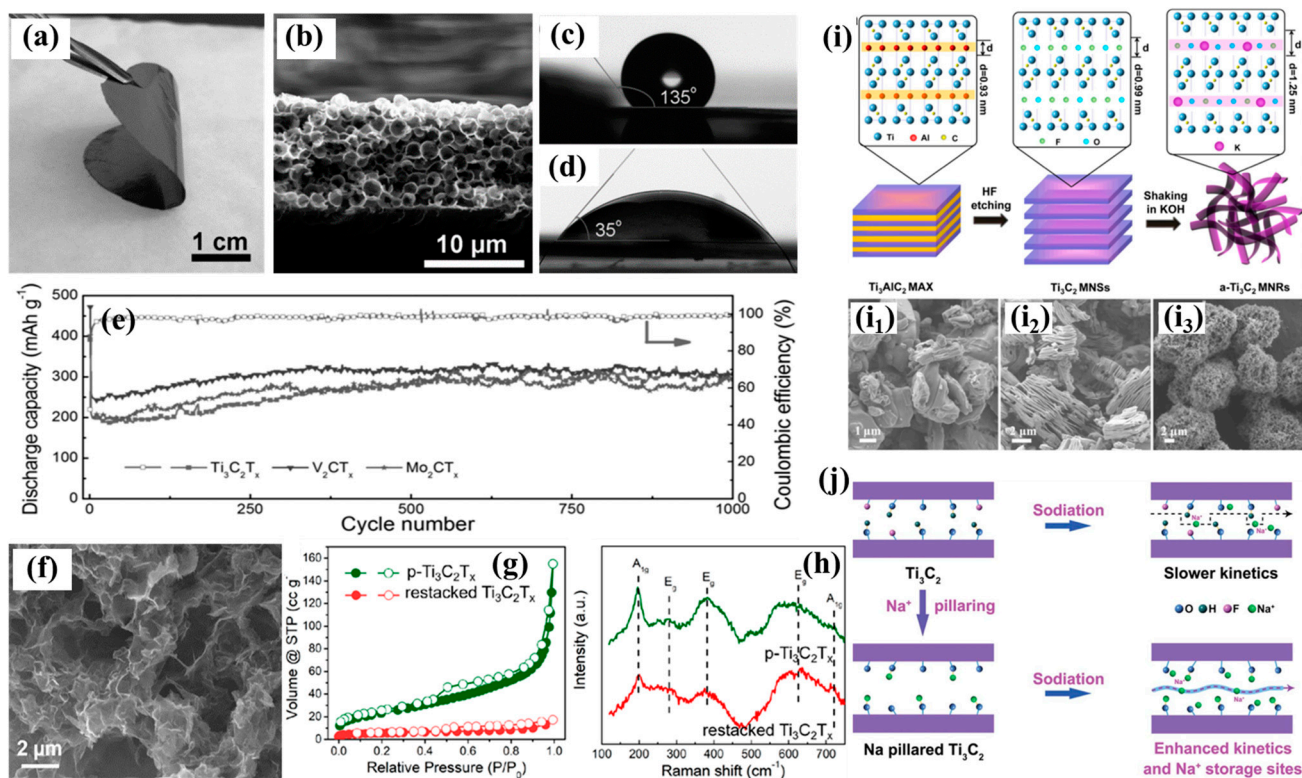


Figure 3. (a) Digital photo, (b) cross-sectional SEM image, and (c) water contact angle of a flexible 3D macroporous $\text{Ti}_3\text{C}_2\text{T}_x$ electrode. (d) Water contact angle of the compact $\text{Ti}_3\text{C}_2\text{T}_x$ electrode. (e) Cyclability of the different electrodes at 2.5 C (reproduced with permission from Ref. [60]; copyright 2017, Wiley-VCH). (f) SEM images of p- $\text{Ti}_3\text{C}_2\text{T}_x$, (g) N_2 isotherm, and (h) the Raman spectra of p- $\text{Ti}_3\text{C}_2\text{T}_x$ and pure restacking $\text{Ti}_3\text{C}_2\text{T}_x$ (reproduced with permission from Ref. [37]; copyright 2021, Wiley-VCH). (i) Schematic of the synthesis of a- Ti_3C_2 MNRs and (i₁–i₃) SEM images. (1) Synthesis of Ti_3AlC_2 ; (2) extraction of the Al layer with 40% HF solution; (3) Ti_3C_2 continuously shaken in KOH solution, producing a- Ti_3C_2 MNRs (reproduced with permission from Ref. [62]; copyright 2017, Elsevier). (j) Schematic of the Na^+ diffusion process in different electrodes (reproduced with permission from Ref. [65]; copyright 2018, Royal Society of Chemistry).

These results showed improvement in the capacity and rate performance of SIBs via effective structural modulation and morphology tuning. Especially for an ultrahigh rate performance, this kind of Na^+ storage material has obvious advantages. However, on the whole, as anodic materials for SIBs, MXenes still have the problems of low specific capacity, lower coulombic efficiency, and high charging voltage (an average voltage of >1.5 V). This significantly reduces the working voltage of the full cell which has a negative impact on the energy density. Therefore, it is very urgent and critical to effectively reduce the discharge–charge potential through effective structural regulation.

3.2. Anode Materials Based on Nonmetal Material/MXenes Composites

Although MXenes have attractive advantages, they are vulnerable to layer stacking due to van der Waals interactions, which are inevitable in 2D materials [31]. This stacking inhibits the accessibility of electrolytes and reduces the charge transfer path, thus damaging the properties of MXenes. In addition, MXenes are very easy to oxidize, for example, in the conversion of the T–C bond into TiO_2 and C, which seriously affects their Na^+ storage activity [31]. In order to overcome these bottlenecks, various strategies have been considered. Among them, it is a very effective strategy to combine them with nonmetal materials with Na^+ storage activity (such as hard carbon, graphene, silicon, black phosphorus, etc.), stabilize their structure, and give play to the advantages of each component. Table 2 presents

different composites based on MXenes, which have significant enhancements due to the introduction of active components compared with the pure MXenes mentioned above.

Table 2. Performance comparison of different nonmetal/MXene composites in SIBs.

Materials	Long-Term Capacity	Current Density	Cycle Number	Rate Performance	Charge Voltage at Medium Capacity	Ref.
HC/MXene	272.3 mAh/g	0.2 A/g	1500	66.7 mAh/g@10 A/g	~0.7 V	[69]
T-MXene@C	139.5 mAh/g	1 A/g	3000	77.8 mAh/g@10 A/g	–	[70]
rGO/p-Ti ₃ C ₂ T _x	~110 mAh/g	1 A/g	2000	~70 mAh/g@5 A/g	~1.5 V	[53]
G-Ti ₃ C ₂ T _x	167 mAh/cm ³	0.5 A/g	2000	112.4 mAh/g@5 A/g	~1.7 V	[71]
Si/MXene microspheres	376 mAh/g	0.1 A/g	500	63 mAh/g@2 A/g	~1.4 V	[72]
Si/MXene@HC	208 mAh/g	0.05 A/g	500	122.5 mAh/g@1 A/g	~1.2 V	[52]
p-Ti ₃ C ₂	80 mAh/g	0.5 A/g	100	~60 mAh/g@1 A/g	~0.8 V	[61]
BPQD/Ti ₃ C ₂	~170 mAh/g	0.2 A/g	100	~150 mAh/g@2 A/g	~1.6 V	[55]
BP/MXenes	658 mAh/g	1 A/g	2000	164 mAh/g@2 A/g	~0.8 V	[73]
MXene/poly	148.4 mAh/g	1 A/g	5000	105 mAh/g@2 A/g	~1.4 V	[74]
PANI/Ti ₃ C ₂ T _x	135.4 mAh/g	2 A/g	10,000	142 mAh/g@5 A/g	~1.5 V	[69]

Hard carbon (HC) is a commercial anodic material used in SIBs. Its volume change limits cyclability significantly. In order to relieve this phenomenon, Sun et al. employed 2D Ti₃C₂T_x as a multifunctional conductive binder to prepare a flexible HC electrode, where the hydrophilic and conductive MXene nanosheets comprised a 3D network (Figure 4a–e) [69]. It effectively optimized the electrode structure and accommodated the volume expansion, leading to a high-capacity electrode (Figure 4f) with a superior cyclability of 1500 cycles with ~270 mAh/g. Zhang et al. directly transformed Ti₃C₂T_x nanosheets into carbon-coated T₃C₂T_x structures (T-MXene@C) via the in situ carbonization of self-polymerized dopamine [70]. The ultrathin carbon coating protected the MXenes from oxidation and aggregation. This active and stable surface modified structure was endowed with very fast charge transfer, leading to a capacity of 257.6 mAh/g with a CE of 56.9% and a superior rate performance of 77.8 mAh/g at 10 A/g, as well as long durability with 3000 cycles. RGO has a certain level of flexibility and strong controllability, and it is easy to assemble with MXene materials. Simultaneously, it can generate rich porous structures in the composite to promote material transport and electron transfer. Zhang et al. prepared nanoporous Ti₃C₂T_x sheets, assembled with RGO and cellulose nanofibers in an elastic, self-supported structure, and this had more accessible surfaces and active sites [53]. The as-prepared composite showed a capacity of 280 mAh/g at 0.1 mA/g with a CE of 54.7% and a cyclability of 1000 cycles. Wei et al. reported a hierarchical porous structure for highly dense Ti₃C₂T_x monoliths involving a porous graphene template. Owing to the superior electron–ion conductivity and transport pathways, the hierarchical structure exhibited 270 mAh/cm³, and the charge capacity could reach 167 mAh/cm³ after 2000 cycles [71].

Si has also been combined with MXenes to enhance the performance of SIBs. Si has a high theoretical capacity of 960 mAh/g via the formation of NaSi, which is higher than Sn (850 mAh/g) and Sb (660 mAh/g) using similar mechanisms, but it is also limited by poor ion diffusion and large volume changes. Thus, Wang et al. designed the advanced flower-like Si/MXene structures, which had superior properties and a high capacity of 751 mAh/g with a CE value of 48.5% (Figure 4g) and 376 mAh/g after 500 cycles [72]. It was observed that part of the capacity contribution was based on the formation of NaSi₆, as shown by the ex situ XRD results in Figure 4h. Gou et al. reported a Si/MXene@HC structure coupled with a carbon-coated Si anode with a conductive MXenes matrix, which also presented an initial CE of 61.8% and a superior cyclability of 500 cycles, and it benefited from the effective relief of volume expansion and a highly conductive structure [52].

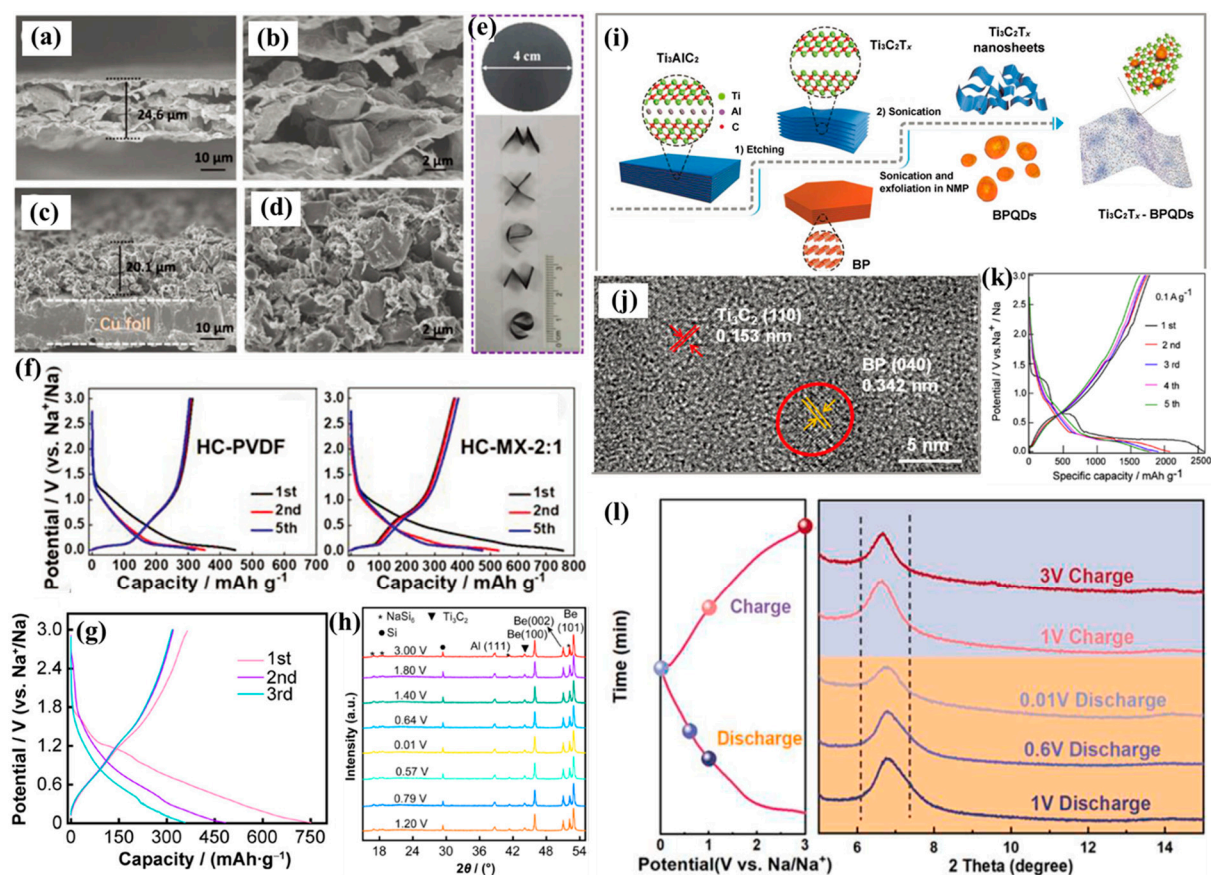


Figure 4. SEM images of (a,b) HC/MXene (HC-MX-2:1) and (c,d) HC/PVDF electrodes; (e) digital photo of flexible HC/MXene film and shaped “MXene” letters. (f) The discharge–charge profiles of HC/PVDF and HC/MXene electrodes at 30 mA/g (reproduced with permission from Ref. [69]; copyright 2019, Wiley-VCH). (g) Discharge–charge profiles and (h) ex situ XRD patterns of different states for Si/Ti₃C₂ composites (reproduced with permission from Ref. [72]; copyright 2022, Springer). (i) Schematic of the formation process and (j) HRTEM image of a BPQD/Ti₃C₂T_x composite (reproduced with permission from Ref. [55]; copyright 2018, Wiley-VCH). (k) Initial five discharge–charge profiles of PDDA-BP/Ti₃C₂ heterostructures (reproduced with permission from Ref. [73]; copyright 2019, Elsevier). (l) Ex situ XRD patterns of sandwich-like MXenes between PEI polymer networks (reproduced with permission from Ref. [74]; copyright 2023, Elsevier).

Black phosphorus (BP) is a promising anodic material due to a high capacity of 2596 mAh/g with alloying reaction mechanisms, ~7 times that of HC. However, it suffers from rapid capacity attenuation caused by a huge volume change of ~300%. Additionally, BP is a semiconductor with poor conductivity that greatly impedes electron and ion transfer. Thus, the combination of BP and MXene can effectively exert their advantages to improve sodium storage properties. Li et al. studied a BP/Ti₃C₂ composite using experiments and DFT calculations [38], and it could form a stable interfacial interaction to reduce the electron and Na⁺ transfer resistances, obtaining an impressive electrochemical performance for SIBs, especially a high discharge capacity of 1280 mAh/g with a CE value of 51.7%. Meng et al. reported a composite made of BP quantum dots and a Ti₃C₂ nanosheet (BPQD/Ti₃C₂) for the purpose of Na⁺ storage via etching assisted by a sonication reaction, as shown in Figure 4i [55], in which BP quantum dots with less size in three dimensions effectively shortened the diffusion length and reduced the huge volume change in the discharge–charge process. Simultaneously, the highly conductive Ti₃C₂ substrate improved the conductivity and led to a fast charge transfer. The Ti–O–P bond in the composite further induced atomic charge polarization and enhanced the pseudocapacitance characteristic. Serving

as the anode of SIBs, it exhibited superior stability with 1000 cycles and a remarkable rate performance (>100 mAh/g). Zhao et al. constructed molecular-level heterostructures by assembling layered BP and Ti_3C_2 [73]. Benefitting the advanced structure with face-to-face contact between the BP and Ti_3C_2 , this novel 2D interlayer provided effective charge transfer and diffusion channels. It displayed high structural stability, with the monodispersed BP in the Ti_3C_2 buffering the volume expansion, showing an ultrahigh capacity of 2588 mAh/g (CE value of 68.7%) with a lower medium charge voltage of ~ 1.2 V (Figure 4k) and an excellent cyclability rate of 658 mAh/g after 2000 cycles.

Furthermore, the strategy of combining MXenes with the polymer is another effective way to enhance performance. Jin et al. designed a $\text{Ti}_3\text{C}_2\text{T}_x$ -based sandwich structure with a stable framework and large interlayer spacing, which depended upon facile self-assembly assisted by a dynamic hydrogen-bonding network made of polyethyleneimine (PEI) [74]. This PEI had rich amino groups, which can form dense polymer hydrogen bonds to further strengthen mechanical strength, and PEI chains can provide extra N sites for Na^+ storage. When the larger Na^+ intercalated the interlayer in the discharge process, it had a little change the in ex-situ XRD patterns (Figure 4l), which ensured the structure stability. As expected, this unique PEI/MXene structure showed excellent cycling performance and enhanced Na^+ storage for 3000 cycles. Similarly, Wang et al. designed a polyaniline/ $\text{Ti}_3\text{C}_2\text{T}_x$ composite via the self-assembly of positively charged conductive polyaniline and $\text{Ti}_3\text{C}_2\text{T}_x$ [75] with enlarged spacing, negative-to-positive transition promotion, and significantly improved ion diffusion kinetics. As a result, it presented an excellent cyclability rate of 10,000 cycles at 2 A/g for SIBs. These results presented a facile strategy for obtaining a superior rate performance and long-term durability in MXene-based materials.

In these nonmetal materials/MXene composites, the properties of some materials improve through the improvement of conductivity, which significantly enhances the cyclability. However, for surface redox reactions and capacitive materials, the battery capacity is obviously low, which is an important defect to a large extent. For Si and P, which can form a similar alloy structure to sodium, their specific capacity is large, and the energy barrier for desodiation is lower. The introduction of MXenes significantly improves their structural expansion and conductivity. If we can further optimize the CE of the initial cycle and increase the material production, it will have great application potential.

3.3. Anode Materials Based on Metal Oxide/MXene Composites

The modification of MXenes by oxides and the surface functionalization of MXenes by oxides are effective in organizing the stacking of MXene laminates. In addition, the structures of MXenes and oxides can also enhance their stability to a certain extent, so that they can avoid oxidation and damage to their structures. At the same time, loading oxides with sodium-ion-storage-active materials on MXenes can further regulate their storage performance, such as capacity, voltage, magnification, etc., which is expected to further develop ideal sodium-ion storage materials. So far, a variety of oxides and MXene composites have been studied; their properties have their own advantages and disadvantages [32]. The following is a summary of several typical structures, and some of the improved parameters are shown in Table 3.

Table 3. Performance comparison of oxide/MXene composites in SIBs.

Materials	Long-Term Capacity	Current Density	Cycle Number	Rate Performance	Charge Voltage at Medium Capacity	Ref.
Na _{0.23} TiO ₂ /Ti ₃ C ₂	56 mAh/g	2 A/g	4000	47 mAh/g@3 A/g	~1.0 V	[76]
TiO ₂ @Ti ₃ C ₂ T _x	116 mAh/g	0.96 A/g	5000	68 mAh/g@3.84 A/g	~1.5 V	[77]
NC/TiO ₂ /Ti ₃ C ₂ T _x	157.5 mAh/g	2 A/g	1900	100.1 mAh/g@10 A/g	~1.2 V	[78]
Hierarchical TiO ₂ /Ti ₃ C ₂	101 mAh/g	0.2 A/g	500	52 mAh/g@2 A/g	~1.6 V	[79]
Pillar-free TiO ₂ /Ti ₃ C ₂	153 mAh/g	0.6 A/g	100	151.5 mAh/g@1 A/g	~1.5 V	[80]
HC-TiO ₂ /MXenes	660 mAh/g	1 A/g	100	250 mAh/g@1 A/g	~0.8 V	[81]
Sb ₂ O ₃ /Ti ₃ C ₂ T _x	472 mAh/g	0.1 A/g	100	295 mAh/g@2 A/g	~1.0 V	[82]
CoNiO ₂ /MXene	223 mAh/g	0.07 A/g	140	188 mAh/g@0.3 A/g	1.3 V	[83]
SnO ₂ /MXene	208.6 mAh/g	0.4 A/g	100	81 mAh/g@2 A/g	1.25 V	[84]
VO ₂ /MXene	280.9 mAh/g	0.1 A/g	200	206 mAh/g@1.6 A/g	~1.5 V	[85]

Attention has been aimed at Ti-based materials due to their acceptable capacity and superior cyclability. Layered titanium-based materials are the candidates for SIBs due to the moderate redox couples of Ti³⁺/Ti⁴⁺, such as Na_{0.23}TiO₂. Huang et al. synthesized a 3D Na_{0.23}TiO₂/Ti₃C₂ composite by growing amorphous Na_{0.23}SiO₂ nanobelts on Ti₃C₂ [76], forming a special sandwich structure, as shown in Figure 5a. Figure 5b presents the first three cycle profiles of Na_{0.23}TiO₂/Ti₃C₂, which provides a lower charge potential. The unique structure was conducive to electrolyte infiltration and rapid ion transfer, and the small-sized Na_{0.23}TiO₂ shortened the diffusion path of Na⁺, benefiting the promotion of the rate performance and ensuring good cyclability. The composites have ultralong stability and can operate for 4000 cycles at 2A/g with a capacity retention of ~100%. Furthermore, TiO₂ has also been thoroughly investigated for use in SIBs due to its low cost, exceptional chemical durability, and safe operation voltage and because it is an environmentally benign material. However, low conductivity limits its rate performance and durability in the discharge–charge process. Many strategies—such as the construction of different nanostructures to shorten ion and electron pathways and the introduction of highly conductive additives to enhance conductivity—have been adopted to address these issues. Based on this, Guo et al. reported a nanocomposite of Ti₃C₂T_x-encapsulated TiO₂ spheres (TiO₂@Ti₃C₂T_x), which served as the anode material for SIBs [77]. The composite material gave the SIBs a superior rate performance and a long cycle. As a result, the composite provided a high capacity of 116 mAh/g at 0.96 A/g with 5000 cycles. Wang et al. demonstrated a crumpled, N-doped, carbon-decorated TiO₂/Ti₃C₂ composite (NC-TiO₂/Ti₃C₂) [78] in which the nano-TiO₂ was dispersed on the conductive network of crumpled Ti₃C₂ with improved electrochemical kinetics. The composite showed an excellent cycling ability of 1900 cycles at 2 A/g and a superior rate performance of 100.1 mAh/g at 10 A/g. Yang et al. reported a layered hierarchical TiO₂/Ti₃C₂ nanohybrid [79] in which nanoscale TiO₂ formed in situ and uniformly dispersed on Ti₃C₂, and it could obtain a CE value of 66% and operate for 500 cycles at 0.2 A/g thanks to its conductivity and ion mobility advantages. Wang et al. prepared pillar-free TiO₂/Ti₃C₂ composites with extended layer spacing via the sintering intercalation of Ti₃C₂ [80]. The TiO₂/Ti₃C₂ composites showed a high capacity of 237.8 mAh/g at 0.1 A/g and an acceptable cyclability rate performance of 100 cycles at 0.6 A/g for SIBs, which were attributed to the extended interlayer fixed by the TiO₂ and the significant synergies between the Ti₃C₂ and TiO₂ with respect to the structural stability, which was investigated using ex-XRD and showed no obvious change in the discharge–charge process (5c). Gao et al. reported a strategy for fabricating an HC–MXene/TiO₂ composite [81], where Ti₃C₂T_x with rich oxygen-containing groups reacted with HC to form a Ti–O–C-covalent-crosslinked HC–Ti₃C₂T_x composite in a ball milling process. The edge of the Ti₃C₂T_x was oxidized to TiO₂ nanorods, forming a regular 1D/2D heterostructure and improving the structural stability. Simultaneously, the Ti₃C₂T_x/TiO₂ heterojunction formed a 3D network and provided more active sites. Consequently, the

as-prepared HC-MXene/TiO₂ exhibited a high capacity of 660 mAh/g and a superior rate performance.

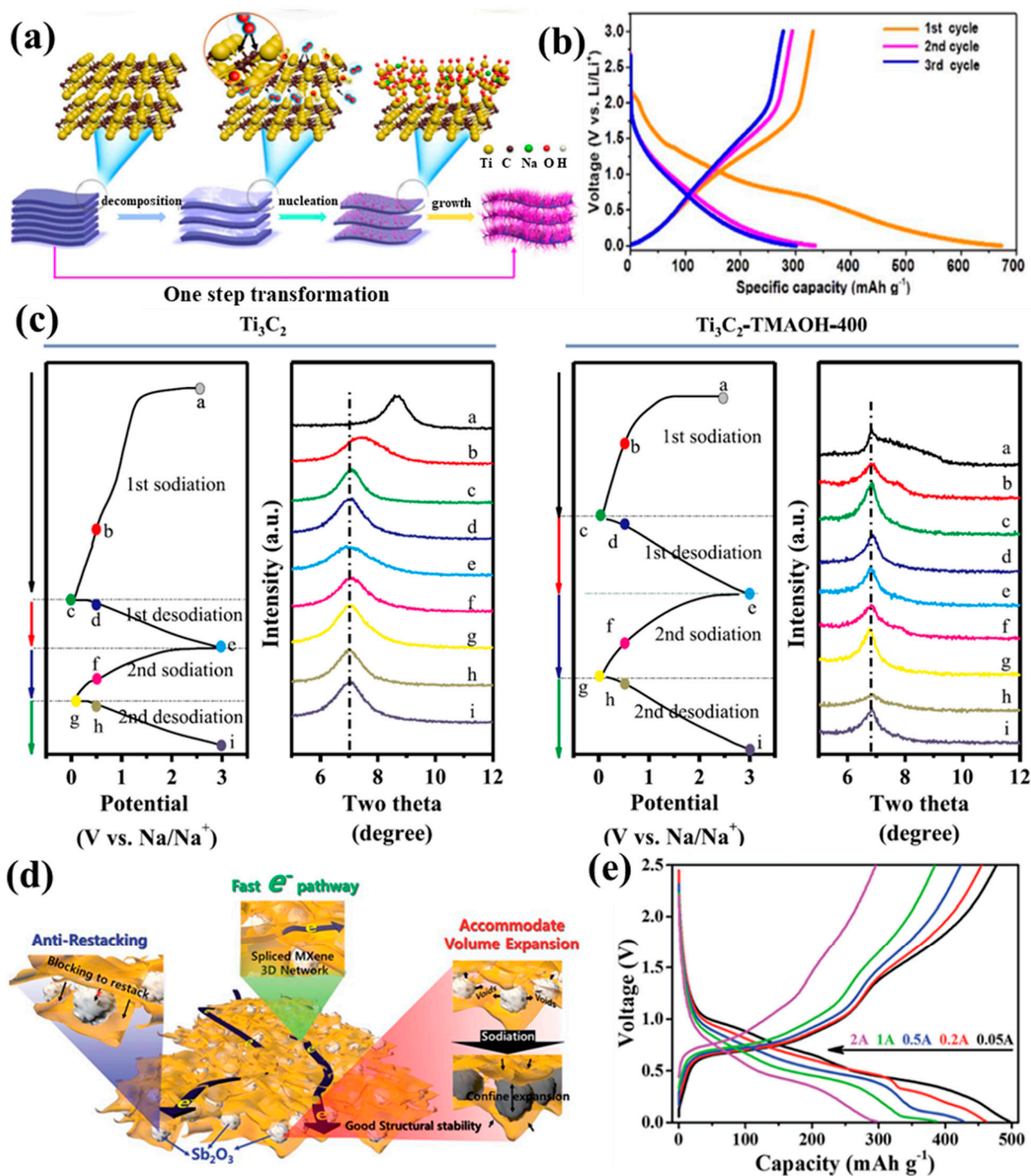


Figure 5. (a) Schematics of the synthesis and (b) discharge–charge profiles for a sandwich-like Na_{0.23}TiO₂/Ti₃C₂ composite (reproduced with permission from Ref. [76]; copyright 2018, Elsevier). (c) Ex situ XRD patterns for Ti₃C₂ and Ti₃C₂-TMAOH-400 upon sodiation and desodiation (reproduced with permission from Ref. [80]; copyright 2020, Elsevier). (d) Schematics of the performance-enhanced mechanism of an Sb₂O₃/MXene electrode in SIBs. (e) Discharge–charge profiles of an Sb₂O₃/Ti₃C₂T_x electrode at different current densities (reproduced with permission from Ref. [82]; copyright 2017, Royal Society of Chemistry).

Sb-based material is also a kind of sodium storage material with high capacity. At the same time, Sb has a suitable voltage (0.5–0.8 vs. Na^+/Na), but its volume changes greatly (~290%) in the discharge–charge process. Therefore, MXene composites can be used to alleviate volume change, enhance electronic conductivity, and promote property improvement. Guo et al. prepared an $\text{Sb}_2\text{O}_3/\text{Ti}_3\text{C}_2\text{T}_x$ composite with high electron conductivity and a high Na^+ diffusion rate [82]. In this architecture, Sb_2O_3 nanoparticles prevent the $\text{Ti}_3\text{C}_2\text{T}_x$ from piling up, and the generated gap can relieve serious volume changes (Figure 5d), maintaining structural stability. The composite has a high capacity of 472 mAh/g at 0.1 A/g with a CE value of 59.6% and a superior rate performance with 295 mAh/g (Figure 5e). CoNiO_2 is a typical transition metal oxide and is widely studied with respect to LIBs, but it is rarely reported in SIBs. Tao et al. prepared a $\text{CoNiO}_2/\text{Ti}_3\text{C}_2\text{T}_x$ composite via the facile hydrothermal method assisted by calcination [83]. The as-prepared $\text{CoNiO}_2/\text{Ti}_3\text{C}_2\text{T}_x$ showed a higher retention of 223 mAh/g at 0.1 mA/g after 140 cycles and a superior rate performance of 188 mAh/g at 0.3 A/g. It was important that the layered $\text{Ti}_3\text{C}_2\text{T}_x$ buffered the volume expansion of CoNiO_2 , promoted ion transfer, and increased the CoNiO_2 active sites for the storage of Na^+ in battery operations.

Among these oxide/MXene composites, the properties of the composites are enhanced by improving the conductivity and alleviating the volume expansion, especially in cyclability. However, the battery capacity is obviously low and is mainly limited by its sodium storage mechanism. If a battery system with high specific capacity cannot be designed based on a sodium storage mechanism, the structural modulation of the materials will have difficulty solving this important disadvantage, which will greatly limit the further applications of oxide/MXene composites in sodium-ion batteries. On the other hand, the low initial CE value is also an important reason to limit the development of these materials.

3.4. Anode Materials Based on Metal Sulfide/MXene Composites

A variety of sulfides have been reported to be used as anode materials for SIBs, mainly including layered sulfide materials and nonlayered materials. Layered materials include MoS_2 [86–88], FeS_2 [89], SnS_2 , and other disulfides [90,91], and nonlayered materials include Sb_2S_3 , CoS , MoS_3 , etc. [92–95], which demonstrates the superior performance of SIBs (Table 4). Among layered sulfides, MoS_2 attracts much attention due to its high energy density. It has a graphite structure bound by a weak van der Waals reaction and is endowed with a high specific surface area and a large ion intercalation space. Even so, the intercalation of Na^+ with a larger radius leads to serious volume expansion, causing lower capacity and poor stability in SIBs. In order to solve this problem, it is very necessary to develop an effective strategy to increase the interlayer spacing of MoS_2 so as to relieve structural damage [42,96]. However, the increased layer spacing could extend the charge transport channel of MoS_2 and result in reduced conductivity, which is not conducive to its properties. Therefore, the combination of highly conductive skeleton materials with MoS_2 is an effective strategy to enhance the performance of SIBs.

Table 4. Comparison of the performance values for different sulfide/MXene anodes in SIBs.

Materials	Long-Term Capacity	Current Density	Cycle Number	Rate Performance	Charge Voltage at Medium Capacity	Ref.
$\text{MoS}_2/\text{Ti}_3\text{C}_2\text{T}_x$	250.9 mAh/g	0.1 A/g	100	162.7@1 A/g	>1.5 V	[97]
$\text{MoS}_2/\text{Ti}_3\text{C}_2\text{T}_x$	331 mAh/g	0.1 A/g	70	186.2@0.8 A/g	>1.5 V	[86]
C- $\text{MoS}_2/\text{CNTs-Ti}_3\text{C}_2$	562 mAh/g	0.1 A/g	200	475@2 A/g	>1.5 V	[98]
$\text{MoS}_2/\text{Ti}_3\text{C}_2\text{T}_x/\text{CKF}$	298 mAh/g	–	300	434.7@1 A/g	~1.8 V	[87]
TH- $\text{MoS}_2/\text{Ti}_3\text{C}_2$	582 mAh/g	1 A/g	600	439.3@5 A/g	>1.5 V	[99]
$\text{MoS}_2@\text{MXene}@\text{TiO}_2$	568.3 mAh/g	2 A/g	100	359.6@5 A/g	>1.5 V	[100]
$\text{Nb}_2\text{CT}_x@\text{MoS}_2@\text{C}$	403 mAh/g	1 A/g	2000	260@40 A/g	>1.5 V	[42]

Table 4. Cont.

Materials	Long-Term Capacity	Current Density	Cycle Number	Rate Performance	Charge Voltage at Medium Capacity	Ref.
Nb ₂ CT _x @MoS ₂	394 mAh/g	1 A/g	1000	196@20 A/g	>1.5 V	[88]
SnS ₂ /MXene	322 mAh/g	0.1 A/g	200	78 mAh/g@2 A/g	~1.7 V	[90]
FeS ₂ /MXene	474.9 mAh/g	5 A/g	600	456.6 mAh/g@10 A/g	~1.4 V	[89]
Co _x Fe _{1-x} S ₂ @S-Ti ₃ C ₂	399 mAh/g	5 A/g	600	596 mAh/g@10 A/g	~1.8 V	[91]
CoS/MXene	267 mAh/g	2 A/g	1700	272 mAh/g@5 A/g	~1.8 V	[92]
SnS/MXene	320 mAh/g	0.5 A/g	100	255.9 mAh/g@1 A/g	~1.45 V	[94]
CuS/MXene	347 mAh/g	3 A/g	800	346.3 mAh/g@8 A/g	~1.7 V	[93]
NiS ₂ /MXene	189 mAh/g	1 A/g	200	147 mAh/g@2 A/g	~1.6 V	[101]
ReS ₂ /MXene	202 mAh/g	2 A/g	200	138 mAh/g@5 A/g	~1.75 V	[102]
MoS ₃ /Ti ₃ C ₂ T _x	611 mAh/g	2 A/g	1000	~370 mAh/g@5 A/g	~2.0 V	[50]
Sb ₂ S ₃ @m-Ti ₃ C ₂ T _x	72 mAh/g	2 A/g	1000	232 mAh/g@1 A/g	~1.25 V	[95]
Sb ₂ S ₃ /Ti ₃ C ₂	464 mAh/g	1 A/g	500	533 mAh/g@2 A/g	~1.0 V	[103]

Wu et al. prepared a MoS₂/Ti₃C₂T_x composite with a layer-by-layer structure [97], in which the increased layer spacing improved the ion accessibility of MXenes and their specific capacity. Serving as a SIB anode, the composite presented a higher initial CE value of ~67% and a capacity of 250.9 mAh/g after 100 cycles. At the same time, it showed a superior rate performance of 162.7 mAh/g at 1 A/g. A composite of Ti₃C₂T_x-modified and -anchored MoS₂ nanosheet, as demonstrated by Du et al., had a high specific capacity and high cycling performance; even after 70 cycles of operation [86], it still showed a high capacity of 331 mAh/g at 100 mA/g, with only 0.058% attenuation per cycle. In this unique structure, the MoS₂ nanosheets anchored on the Ti₃C₂T_x shortened the ion diffusion path and provided more electroactive sites toward Na⁺, and the improved specific area facilitated electrolyte–electrode contact. He et al. reported a facile one-pot strategy to prepare a 1D/2D heterostructure [98], where ultrathin carbon-layer-coated MoS₂ nanosheets with expanded interlayer spacing vertically grew on Ti₃C₂ and crosslinked carbon nanotubes (C-MoS₂/CNTs-Ti₃C₂) served as the 3D conductive network. The developed quaternary composite showed a high initial CE value of 72%, an advanced performance with 562 mAh/g after 200 cycles, and a superior rate performance of 475 mAh/g at 2 A/g. The DFT results demonstrated that a combined MoS₂ and Ti₃C₂ matrix could optimize the adsorption energy toward Na⁺, which enhanced the Na⁺ storage capability, as shown in Figure 6a. Zhang et al. proposed a multilayer composite with a nano-/microstructure formed by self-assembled MoS₂ nanoflowers, MXene, and hollow carbon kapok fibers (MoS₂/Mxene/CKF) [87]. The nano-/microstructure was connected to form a heterostructure and avoided agglomeration, leading to improved conductivity and structural stability. Benefitting from these, it presented a high initial CE value of 80% and a higher specific capacity, as shown in Figure 6b, as well as a better rate performance (639.3 and 434.7 mAh/g at 0.05 and 1 A/g). The ex situ XRD patterns exhibited changes of (002) in the MoS₂, which shifted to a low angle in the discharge and recovered to the original position due to Na deintercalation with high reversibility due to the rational design. Wen et al. designed a simple intercalation vulcanization strategy to construct TH-MoS₂/Ti₃C₂ heterostructures with closely stacked and layered structures, which provided a facile way to synthesize layered heterostructure composites by stacking different 2D materials [99]. The TH-MoS₂/Ti₃C₂ anode showed a high initial CE of 83.4%, a capacity of 743.6 mAh/g, and an excellent rate performance of 439.3 mAh/g at 5A/g. In addition, Zhang et al. reasonably designed and built a nanocomposite of MoS₂ on layered, porous Ti₃C₂T_x MXene with partial rutile oxide and anatase dual-phase TiO₂ (MoS₂@MXene@TiO₂) [100], which increased the lattice spacing of the vertical arrangement. This unique “plane-to-surface” structure prevented the aggregation and restacking of MoS₂ while also achieving sufficient electrode–electrolyte interactions. At the same time, the heterostructure between two-phase TiO₂, MoS₂, and Ti₃C₂T_x can form a built-in electric field to promote Na⁺ transfer. Therefore, the MoS₂@MXene@TiO₂ heterostructure has an admirable and reversible capacity of 359.6 mAh/g at 5A/g and

shows excellent electrochemical performance in Na^+ full cells coupled with $\text{Na}_3\text{V}_2(\text{PO}_4)_3$ cathodes.

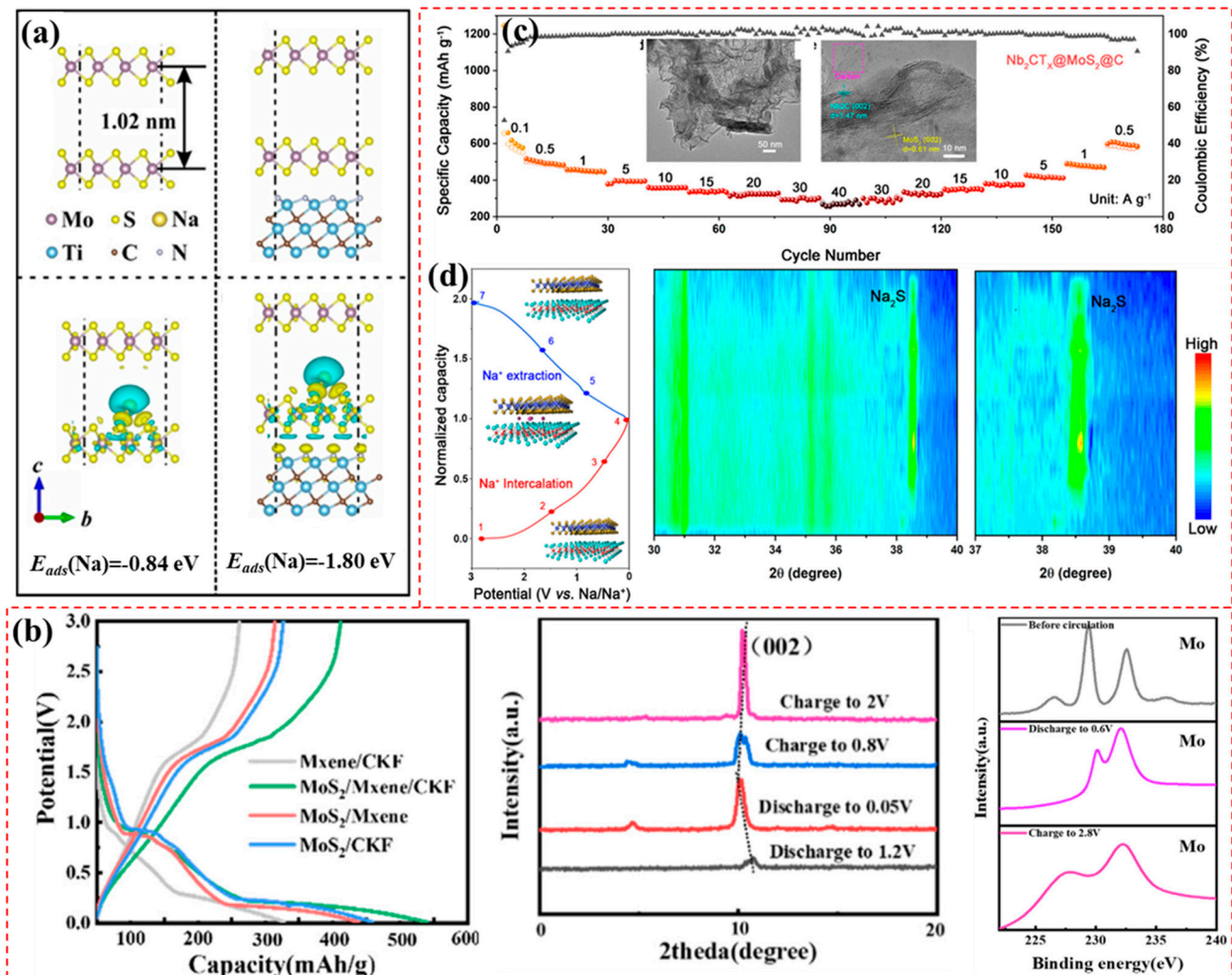


Figure 6. (a) The optimized structure and corresponding adsorption energy of extended MoS₂ and MoS₂/Ti₃C₂ (reproduced with permission from Ref. [98]; copyright 2022, Elsevier). (b) The initial discharge–charge profiles, XRD patterns, and XPS of a MoS₂/MXene/CKF electrode at different depths (reproduced with permission from Ref. [87]; copyright 2022, Elsevier). (c) Rate performance of Nb₂CT_x@MoS₂@C. The TEM and HRTEM images are shown in the insets. (d) Discharge–charge curves of Nb₂CT_x@MoS₂@C at 0.01–3.0 V and the corresponding contour maps of the in situ XRD (reproduced with permission from Ref. [42]; copyright 2021, American Chemical Society).

Yuan et al. developed a carbon-coated Nb₂CT_x MXene/MoS₂ nanocomposite (Nb₂CT_x@MoS₂@C) [42] in which a 3D crosslinking structure was constructed (insets of Figure 6c). In this design, the highly conductive Nb₂CT_x nanosheet prevented the MoS₂ from restacking and provided an effective channel for charge transfer. In addition, the carbon coating had a certain level of volume elasticity and improved conductivity, ensuring the insertion of Na⁺ and promoting rapid dynamics and long-term durability. Consequently, the Nb₂CT_x@MoS₂@C composite provided 530 mAh/g and excellent cyclability after 2000 cycles at 1A/g, as well as a CE of 58%. Most importantly, as shown in Figure 6c, the Nb₂CT_x@MoS₂@C anode could realize rapid a discharge–charge process with capacities of 340 and 260 mAh/g at 20 and 40 A/g, respectively. The in situ XRD (Figure 6d) shows that the XRD peaks were not shifts in the Na⁺ intercalation, and there was a new Na₂S phase due to the expanded layered spacing and an extra Na⁺ storage mechanism, which is

promising for the practical applications. Recently, the same researchers fabricated hollow MoS_2 /carbon spheres bound by Nb_2CT_x , obtaining a capacity of 196 mAh/g at 20 A/g. A DFT simulation showed that, under this material design strategy, Na^+ has a small diffusion barrier [88].

SnS_2 is also a typical layered structure, where the sulfur atoms are tightly packed to form two layers that react via a weak van der Waals force [90]. The larger layer spacing in SnS_2 is conducive to the transport of Na^+ , and it can also combine with Sn atoms to form the NaSn alloy. However, similar to the previous results, the volume expansion is still the main bottleneck limiting its stability, and an effective strategy to build a stable and highly conductive heterostructure is required. Thus, Wu et al. developed self-assembled heterostructures made of MXene and SnS_2 nanosheets [90]. The reversible capacity of MXene@ SnS_2 can reach up to 322 mAh/g after 200 cycles with an initial CE value of 55.2%, which is superior to pure MXenes and other composites. Layered FeS_2 has a similar structure to that of SnS_2 . Unlike SnS_2 , in the mechanism of Na^+ storage, FeS_2 is mainly dependent on intercalation between layers and capacitance contribution, and it cannot form alloys. Huang et al. developed a novel [89], low-destructive, and universal strategy for preparing the heterostructure of sulfide/ $\text{Ti}_3\text{C}_2\text{T}_x$ using Lewis acid molten salt etching, combined with subsequent in situ sulfurization. In particular, as shown in Figure 7a,b, the FeS_2 /MXene structures show a high initial CE value of 86%, a specific capacity of ~700 mAh/g with a lower medium charge potential (~1.25 V), an excellent rate performance of 456.6 mAh/g at 10 A/g, and a superior durability of 474.9 mAh/g at 5 A/g after 600 cycles. It was impressive that a Na^+ full cell with a $\text{Ti}_3\text{C}_2\text{T}_x$ / FeS_2 anode provided 431.6 mAh g^{-1} of reversible capacity at 3 A/g after 1000 cycles. In this unique structure, it benefited from interface electron coupling between $\text{Ti}_3\text{C}_2\text{T}_x$ and FeS_2 (Figure 7c–e); the heterostructure had significantly improved electron conductivity and a stronger adsorption reaction toward Na^+ , and it promoted Na^+ transfer dynamics, as well as a stable structure. Zang et al. reported on bimetal sulfide $\text{Co}_x\text{Fe}_{1-x}\text{S}_2$ /S-doped Ti_3C_2 nanocomposites ($\text{Co}_x\text{Fe}_{1-x}\text{S}_2$ @S- Ti_3C_2) [91] where the interconnected 3D framework was composed of Ti_3C_2 nanosheets, effectively buffering any volume expansion and enhancing the charge transfer. The S- Ti_3C_2 nanosheets provided rich sites for Na^+ storage and inhibited S-loss in the discharge–charge process, which led to increased capacity and cycling stability. As expected, the nanocomposite presented a high CE value of 86% and a superior rate performance with 399 mAh/g at 5 A/g, as well as a durability of 600 cycles.

Nonlayered sulfides such as CoS, SnS and Sb_2S_3 also have high specific capacities, but their conductivities seriously limited their performance [26,50,92–95,101,102,104]. The theoretical capacity of CoS is relatively high, and the Co-S bond is weak, which determines the potential of CoS to be applied to SIBs. Zhang et al. prepared a CoS/ Ti_3C_2 nanocomposite with small CoS nanoclusters anchored on 2D $\text{Ti}_3\text{C}_2\text{T}_x$ (Figure 7f) by combining their advantages [92], especially their advantages in improving conductivity. The capacity of the CoS/MXene could reach to ~400 mAh/g with a high voltage of ~1.8 V (Figure 7g), and it had a superior durability of 267 mAh/g at 2 A/g even after 1700 cycles (Figure 7h). SnS is also an attractive anode material for SIBs because of its high theoretical capacity of 1022 mAh/g and its low cost, but its further applications are limited by low conductivity and serious volume expansion. To this end, Zhang et al. constructed a nanocomposite of MXene-loaded SnS nanoparticles (SnS/MXene) with a CE value of 70.6% and a capacity of 255.9 mAh/g, even at 1 A/g, with improved conductivity [94]. However, in the high current density, it seemed that the sodium storage effect of alloying did not occur, and it was associated with a lower specific capacity, similar to that of oxide. In addition, Sb_2S_3 is an ideal candidate owing to its high theoretical capacity of 946 mAh/g in SIBs. Zhang et al. reported Sb_2S_3 / $\text{Ti}_3\text{C}_2\text{T}_x$ composites with different nanostructures for Na^+ storage [95], indicating that volume expansion was effectively suppressed by $\text{Ti}_3\text{C}_2\text{T}_x$. Wang et al. reported on an Sb_2S_3 / Ti_3C_2 nanocomposite created by covalently bonding Ti-O-Sb and S-Ti and uniformly pinning monodispersed Sb_2S_3 on a $\text{Ti}_3\text{C}_2\text{T}_x$ surface [104]. The construction of effective interfacial chemical bonds could reduce the physical gap between

Sb_2S_3 nanoparticles and $\text{Ti}_3\text{C}_2\text{T}_x$, improving the efficiency of interfacial charge transfers. In addition, interfacial covalent bonds can also effectively limit Sb_2S_3 nanoparticles and corresponding reduction products to the surface of $\text{Ti}_3\text{C}_2\text{T}_x$. Thus, this $\text{Ti}_3\text{C}_2\text{T}_x$ - Sb_2S_3 anode presented a CE value of 68.4% and provided 475 mAh/g of high capacity at 0.2 A/g after 300 cycles, or even 1.0 A/g after 500 cycles of 410 mAh/g. However, it is easy to oxidize $\text{Ti}_3\text{C}_2\text{T}_x$ with the in situ solvothermal method, which has been reported widely, and this sacrifices its conductivity, inhibiting the rapid discharge–charge process. To address this issue, Yang et al. reported a free-standing, flexible, and high-capacity membrane consisting of a $\text{Sb}_2\text{S}_3/\text{Ti}_3\text{C}_2\text{T}_x$ nanocomposite for rapid and stable Na^+ storage, in which 1D Sb_2S_3 nanowires uniformly anchored on $\text{Ti}_3\text{C}_2\text{T}_x$ nanosheets served as Na^+ storage [103] and supported 2D $\text{Ti}_3\text{C}_2\text{T}_x$ to form 3D channels to promote electrolyte infiltration. At the same time, the 2D conductive $\text{Ti}_3\text{C}_2\text{T}_x$ nanosheet enhanced electron transport and limited Sb_2S_3 volume expansion in the discharge–charge process with high reversibility (Figure 7i), as determined with ex situ XPS, as well as the inhibition of discharged sodium polysulfide dissolution caused by chemical absorption and physical constraint, as shown in Figure 7j). In a combination of these effects in 1D Sb_2S_3 and 2D MXene, the obtained composite anodes showed a superior rate performance of 553 mAh/g at 2 A/g and 5000-cycle-long cyclability, as well as an initial CE value of 63.4%. It was confirmed that these strategies could provide more useful insights for the rational structural design of advanced SIB anode materials.

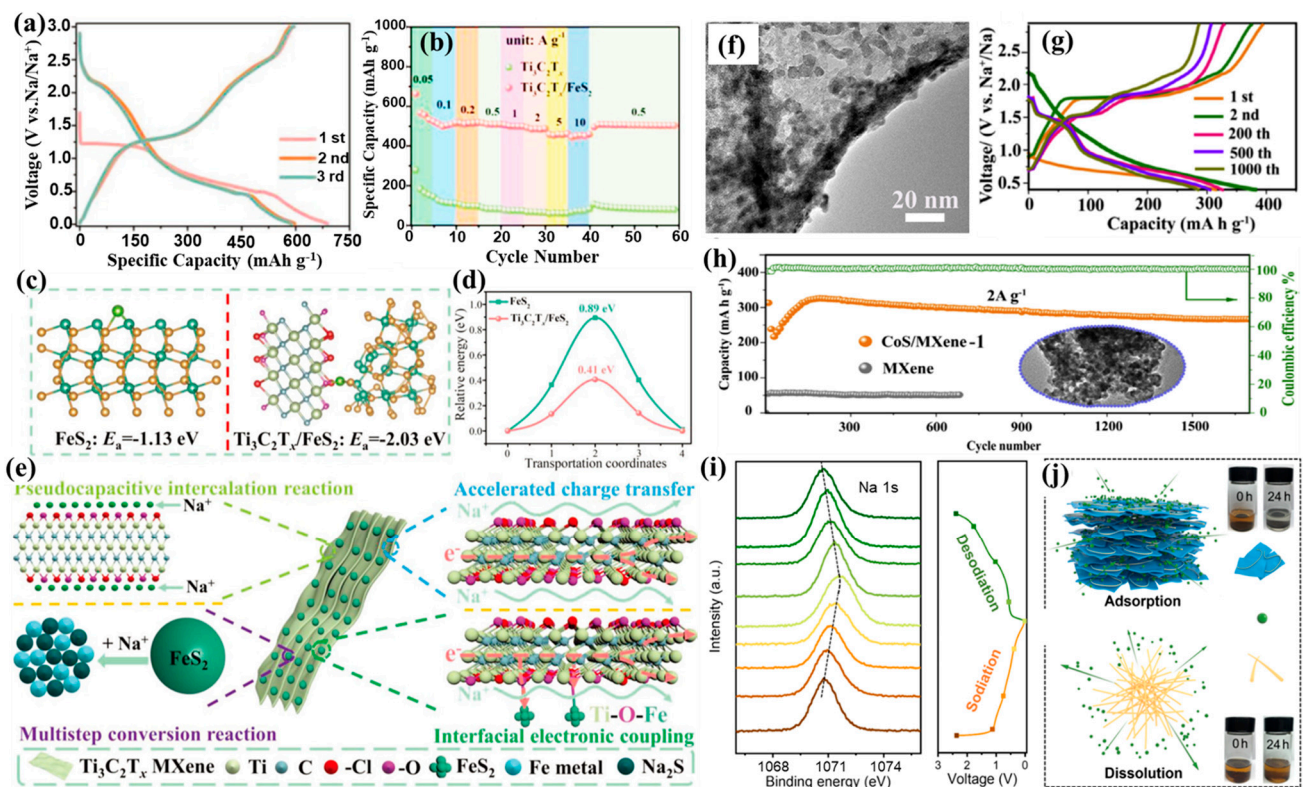


Figure 7. (a,b) Discharge–charge profiles and rate performance of a $\text{Ti}_3\text{C}_2\text{T}_x/\text{FeS}_2$ electrode. (c,d) The Na adsorption energy and Na migration energy barriers of $\text{Ti}_3\text{C}_2\text{T}_x/\text{FeS}_2$ and FeS_2 . (e) Schematics of Na storage behavior with a $\text{Ti}_3\text{C}_2\text{T}_x/\text{FeS}_2$ heterostructure and an underlying mechanism (reproduced with permission from Ref. [89]; copyright 2022, Wiley-VCH). (f) TEM images, (g) discharge–charge curves at 2A/g, and (h) cyclability at 2A/g of CoS/MXene (reproduced with permission from Ref. [92]; copyright 2019, Elsevier). (i) Na 1s spectra of $\text{Sb}_2\text{S}_3/\text{Ti}_3\text{C}_2\text{T}_x$ electrodes and the corresponding sodiation–desodiation profiles. (j) Schematic and digital photo of the adsorption effects of $\text{Sb}_2\text{S}_3/\text{Ti}_3\text{C}_2\text{T}_x$ and Sb_2S_3 on polysulfides. Inset images show the Na_2S_x adsorption effect before and after 24 h (reproduced with permission from Ref. [103]; copyright 2021, Springer).

In the sulfide composite structure, due to the change in the sodium storage mechanism, the composite materials all showed significantly increased specific capacities and enhanced cycle stabilities. Especially in the initial coulombic efficiency, the layered sulfide and high-conductivity structure can be raised to more than 80 (up to 86%), which is comparable to commercial hard carbon. The main problem is that the charging voltage is high, and the average charging voltage is >1.25 V. Therefore, it is necessary to further optimize the structure and composition to reduce the charging voltage.

3.5. Anode Materials Based on Other MXene Composites

There are other composites based on MXenes used in SIBs, such as $\text{CoSe}_2/\text{Ti}_3\text{C}_2\text{T}_x$, $\text{MoSe}_2/\text{Ti}_3\text{C}_2\text{T}_x$, $\text{FePS}_3/\text{Ti}_3\text{C}_2\text{T}_x$, $\text{FeVO}_4/\text{Ti}_3\text{C}_2\text{T}_x$, $\text{NaTi}_2(\text{PO}_4)_3/\text{Ti}_3\text{C}_2\text{T}_x$, $\text{Bi}/\text{Ti}_3\text{C}_2\text{T}_x$, $\text{Sb}/\text{Ti}_3\text{C}_2\text{T}_x$, $\text{CoP-NC}/\text{Ti}_3\text{C}_2\text{T}_x$, and MXene-derived materials [103,105–118]. All the performance values of the composites are summarized in Table 5. For example, Xu et al. reported a hierarchical structure for sheet–tube–dots made of $\text{CoSe}_2@\text{CNTs-MXene}$ [107] that was conducive to fast electrons and ion migration. It presented a high specific capacity of 400 mAh/g at 2 A/g after 200 cycles. A DFT investigation disclosed that the $\text{CoSe}_2@\text{CNTs-MXene}$ contributed to stable Na^+ storage owing to strong adsorption from the hierarchical structure toward polyselenide, avoiding the shuttling effect, and weak interaction between the electrode interface and electrolyte. Tan et al. developed a carbon-coated $\text{MoSe}_2/\text{MXene}$ heterostructure ($\text{MoSe}_2/\text{Mo}_2\text{CT}_x/\text{C}$) [106] where the Mo_2CT_x covered MoSe_2 nanoparticles, and the loose carbon linked the coated species and generated a rich porous structure for the mass transport. $\text{MoSe}_2/\text{Mo}_2\text{CT}_x/\text{C}$ served as a high-performance Na^+ storage material, which presented a CE value of 47% and exceptional cyclability with 2200 cycles, after which the specific capacity could still reach up to 600 and 200 mAh/g at 0.5 and 2 A/g. Ding et al. constructed a novel 2D/2D heterojunction ($\text{FePS}_3/\text{Ti}_3\text{C}_2\text{T}_x$) of layered FePS_3 nanosheets and $\text{Ti}_3\text{C}_2\text{T}_x$ using in situ self-assembly [119], which effectively increased the electron conductivity and specific surface area, promoting a surface–interface charge transfer and alleviating the volume change. The ultrathin, $\text{Ti}_3\text{C}_2\text{T}_x$ -coated, few-layered FePS_3 nanosheets provided a higher 676.1 mAh/g capacity at 0.1 A/g after 90 cycles.

Table 5. Comparison of the performance values of different anode materials in SIBs.

Materials	Long-Term Capacity	Current Density	Cycle Number	Rate Performance	Charge Voltage at Medium Capacity	Ref.
$\text{CoSe}_2@\text{CNTs-MXene}$	400 mAh/g	2 A/g	200	347.5 mAh/g@5 A/g	~1.75 V	[107]
$\text{Co}_{0.5}\text{Ni}_{0.5}\text{Se}_2/\text{Ti}_3\text{C}_2$	338 mAh/g	1 A/g	600	337 mAh/g@3 A/g	~1.75 V	[108]
$\text{SnSe}_2/\text{Ti}_3\text{C}_2\text{T}_x$	245 mAh/g	1 A/g	445	192 mAh/g@5 A/g	~1.5 V	[105]
$\text{MoSe}_2/\text{Mo}_2\text{CT}_x/\text{C}$	484.4 mAh/g	1 A/g	2200	330.6 mAh/g@10 A/g	~1.5 V	[106]
$\text{FePS}_3@\text{MXene}$	676.1 mAh/g	0.1 A/g	90	449 mAh/g@5 A/g	~1.6 V	[119]
$\text{FeVO}_4/\text{MXene}$	105 mAh/g	5 A/g	5000	98 mAh/g@10 A/g	~1.5 V	[117]
$\text{NaTi}_2(\text{PO}_4)_3/\text{Ti}_3\text{C}_2$	~65 mAh/g	2 A/g	2000	~67 mAh/g@2 A/g	~1.25 V	[114]
MXene@NTP-C	~110 mAh/g	5 A/g	10,000	102 mAh/g@10 A/g	~2.0 V	[118]
$\text{Ag-Nb}_2\text{CT}_x$	187 mAh/g	5 A/g	2000	188 mAh/g@5 A/g	~1.6 V	[112]
$\text{Sb}/\text{p-Ti}_3\text{C}_2\text{T}_x$	216.8 mAh/g	0.2 A/g	300	126.6 mAh/g@2 A/g	~0.9 V	[115]
$\text{Ti}_3\text{C}_2\text{T}_x@\text{Sb}$	148 mAh/g	1 A/g	8000	127 mAh/g@2 A/g	~1.2 V	[116]
Bi/MXene	301 mAh/g	5 A/g	2500	307 mAh/g@8 A/g	~0.65 V	[120]
$\text{CoP-NC}/\text{Ti}_3\text{C}_2\text{T}_x$	101.6 mAh/g	0.5 A/g	500	64.1 mAh/g@1.5 A/g	–	[113]
$\text{VS}_4@\text{L-Ti}_3\text{C}_2\text{T}_x$	599 mAh/g	1 A/g	40	33 mAh/g@5 A/g	~1.6 V	[121]
$\text{TiS}_2@\text{C}_{\text{pvp}}$	321.4 mAh/g	10 A/g	5000	339 mAh/g@10 A/g	~1.65 V	[111]
$\text{NaTi}_{1.5}\text{O}_{8.3}$	~140 mAh/g	0.2 A/g	150	101 mAh/g@2 A/g	~0.65 V	[109]
$\text{M-TiO}_2@\text{rGO}$	123.3 mAh/g	5 A/g	5000	142 mAh/g@2 A/g	~1.75 V	[110]
$\text{Na}_2\text{Ti}_3\text{O}_7@\text{C}$	119 mAh/g	2 A/g	200	115 mAh/g@2 A/g	~0.75 V	[122]

Xu et al. prepared flexible free-standing $\text{FeVO}_4/\text{Ti}_3\text{C}_2\text{T}_x$ composite films using facile vacuum filtration [117], which consisted of $\text{Ti}_3\text{C}_2\text{T}_x$ nanosheets and FeVO_4 nanorods. This presented a superior performance with a high capacity for Na^+ storage, which reached up to 129 mAh/g at 5 A/g and maintained a capacity retention rate of 81.1% even after 5000 cycles. Combined with capacitance-type and battery-type electrochemical behaviors, Yang et al. developed a dual-mode Na^+ storage composite made of Ti_3C_2 -nanosheet-

loaded $\text{NaTi}_2(\text{PO}_4)_3$ cubes (MXene@NTP-C) for SIBs [118]. The nanocomposite showed an obviously increased specific capacity (Figure 8a)—more than two times that of pure MXenes—a 49% capacity retention at 10 A/g, and an outstanding cyclability of 10,000 cycles at 5 A/g, as well as a high CE value of ~90%. These are the two battery types in Figure 8a, which were contributed to by the capacitance shown in Figure 8b, the pseudocapacitive manner of MXene, and the diffusion-controlled battery type in the lattice of $\text{NaTi}_2(\text{PO}_4)_3$, such as the site of M_2 , which illustrated the high performance of these SIBs due to their unique properties.

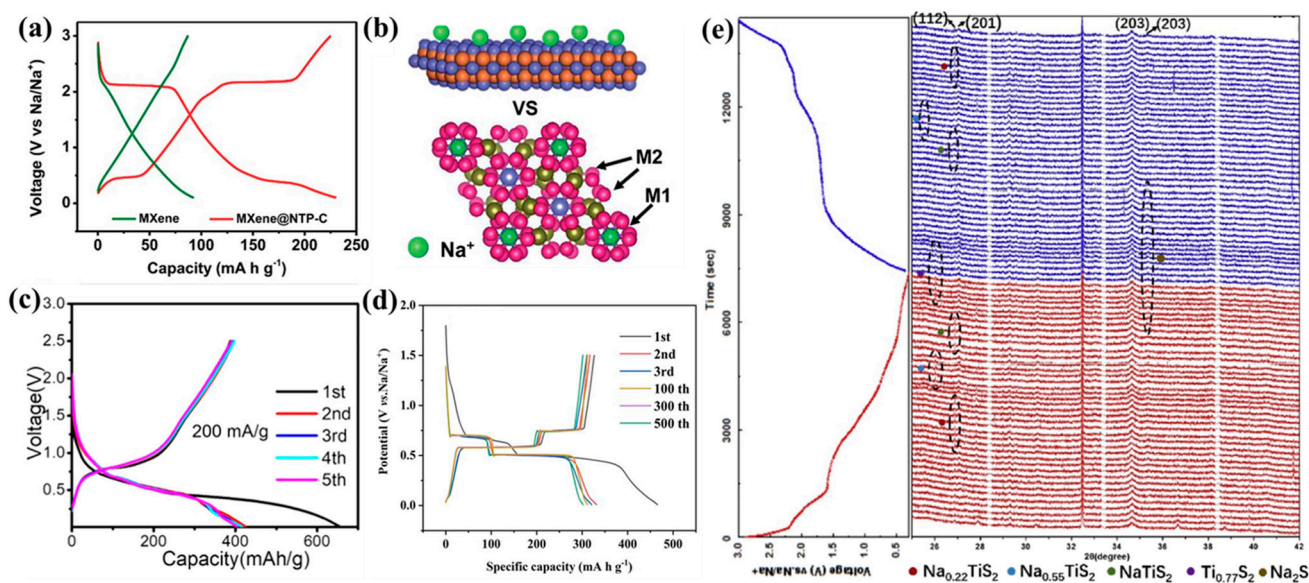


Figure 8. (a) The discharge–charge profiles of pure MXene and MXene@NTP-C. (b) Schematic comparison of the Na^+ storage behavior in $\text{NaTi}_2(\text{PO}_4)_3$ and MXenes (reproduced with permission from Ref. [118]; copyright 2018, Royal Society of Chemistry). (c) The discharge–charge profiles of Sb/p- $\text{Ti}_3\text{C}_2\text{T}_x$ (reproduced with permission from Ref. [115]; copyright 2021, American Chemical Society). (d) Discharge–charge profiles of Bi/MXene anode at different cycles (reproduced with permission from Ref. [120]; copyright 2021, Wiley-VCH). (e) In situ XRD patterns of a $\text{TiS}_2@\text{C}_{\text{pvp}}$ electrode at the first discharge–charge process (reproduced with permission from Ref. [111]; copyright 2020, Elsevier).

As mentioned earlier, Sb can store sodium via alloying. To deliver high-capacity Sb and a superior rate performance for MXenes in SIBs at the same time, Zhang et al. prepared Sb-pillared $\text{Ti}_3\text{C}_2\text{T}_x$ composites (Sb/p- $\text{Ti}_3\text{C}_2\text{T}_x$) with ultrathin Sb particles decorated with few-layered $\text{Ti}_3\text{C}_2\text{T}_x$ nanosheets [115]. Due to the enhanced kinetics achieved by the p- $\text{Ti}_3\text{C}_2\text{T}_x$ and ultrathin Sb particles, the Sb/p- $\text{Ti}_3\text{C}_2\text{T}_x$ exhibited a lower charge potential (Figure 8c), an acceptable capacity of 438.1 mAh/g at 0.05 A/g, and a higher capacity retention of 126.6 mAh/g at 2 A/g, as well as a CE value of 60.6%. Bi with the same reaction mechanism as Sb and with an alloy-type sodium storage mechanism was also used to improve the sodium storage performance and served as the anode material, and it was employed as a promising, fast-charging material for SIBs owing to its excellent rate performance. Ma et al. designed a 2D Bi/MXene composite based on a hydrogen thermal reduction strategy [120] that exhibited a lower charge potential of ~0.65 V (Figure 8d), a superior cyclability of 2500 cycles at 5 A/g, and an excellent rate performance of 307 mAh/g at 8 A/g, as well as a high CE value of 76%. In a full cell based on a $\text{Na}_3\text{V}_2(\text{PO}_4)_3$ cathode, it demonstrated an ultrafast discharge–charge process in 7 min only and an excellent cyclability (>7000 cycles). It could be a promising anode material with a fast discharge–charge capability, and it could be very beneficial to the development of high-rate SIBs.

In addition to using composites with MXenes to improve material conductivity and alleviate volume expansion, some studies have used the unique structure of MXenes to synthesize derivatives using in situ reactions, such as TiO_2 , TiS_2/C , etc. For example, Tang et al. synthesized carbon-coated TiS_2 nanosheets using the in situ vulcanization of polyvinyl-pyrrolidone-modified $\text{Ti}_3\text{C}_2\text{T}_x$, and it presented an outstanding electrochemical performance in SIBs [111]. An ultrathin nanostructure with large interlayer spaces provided easy Na^+ access, leading to a reduced entropic barrier for the reversible conversion and, thus, an ultrafast rate capability and high reversibility, as determined using in situ XRD (Figure 8e), which was based on the conversion of $\text{Ti}_{0.77}\text{S}$ and Na_2S . The unique structure presented a high CE value of 87.6%, a superior rate performance of 387 mAh/g—even at 10 A/g—a high discharge capacity of 448 mAh/g, and a superior cyclability of 5000 cycles. Furthermore, as shown in Table 5, there are various MXene-based composites with superior rate performance and high capacity, and they benefit from effective structure modulation. All these studies could shed light on the development of ultrathin structures combined with high-conductivity substrates for the creation of high-performance SIBs. They could also expand the application of 2D hybrid materials in the energy storage field.

4. Current Issues and Challenges

MXene-based composites with rational structure modulations enhance the performance of SIBs, including their increased specific capacities, and they promote superior rate performance and cyclability, which are mainly dependent on increased conductivity and the facilitation of mass transport. Typical hard carbon anodic materials present a reversible specific capacity of ~ 300 mAh/g with a CE of $\sim 80\%$, a superior rate performance of up to 10C, and excellent cyclability. Especially in high specific capacity, they have low-voltage (<1.5 V) desodiation, showing a 50% desodiation capacity of around 0.2 V. For MXene-based anodic materials, the capacity and rate performance, as well as the cyclability, can reach a high standard of practical application with superior properties compared with hard carbon. However, high charge voltage and lower coulombic efficiency are the main issues hindering further applications. As we show above, the majority of MXene-based materials have a high charge voltage of >1.5 V, or even 1.8 V, which would cause a significant energy density reduction of about 20–30% when matched with the same cathode. Another main challenge is that the scale-up production of MXene-based composites, whose performance is strongly related to MXenes and their composed structure, needs strict synthetic conditions, as well as the use of a large number of F-containing reagents. This is still inefficient on a large scale with respect to single-layer or few-layer MXenes. Furthermore, the stability of MXenes and MXene-based materials is more important, and this can affect the surface structure of composites and determine their electrochemical performance to a great extent. There are a lot of oxygen-containing terminals on the surfaces of MXenes, and MXenes are sensitive to air. During heat treatment, these species are very easy to convert into oxides. On the one hand, this will change the structure of the MXene substrate and optimize the material's conductivity. Simultaneously, the generated oxides will restrict the further loading of highly active components, weaken the interaction between the loaded material and the highly conductive substrate, and are not conducive to structural modulation or electron transfer between components. Therefore, when it comes to MXene-based materials, such as novel Na^+ storage materials, it will be a very urgent and critical task to effectively reduce the issues and challenges through rational and effective structural regulation.

5. Summary and Future Perspectives

This paper introduced applications for MXenes and their composites in the anodes of SIBs. Many studies have been conducted on modified MXenes, oxides/MXenes, sulfides/MXenes, etc. Compared with MXenes and other materials, composites display excellent electrochemical performance. Among them, some strategies for composite structural designs, such as 3D porous MXenes, heterostructures, integrated structures, and in situ conversion ultrathin 2D/1D nanostructures, could provide significant application potential

in the future. As promising 2D structures, MXenes have great research value. Here, we introduced MXenes and their composite structures with different structures, summarized their structural design strategies and battery performance in Na⁺ storage materials, and clarified the structure–activity relationship between highly conductive two-dimensional structures in terms of large-radius sodium-ion storage, especially the unique role of ion transport and volume expansion. At the same time, this study also points out the direction for us to reasonably design structures for high-performance anode materials in SIBs. Even so, at present, MXene-based materials still face the following challenges in Na⁺ storage: (1) the lack of a green large-scale synthetic method for monolayer and few-layer MXenes; (2) the poor stability of MXenes and MXene-based materials; (3) the higher charge voltage in MXene-based materials; (4) and the related lower specific capacity and coulombic efficiency, as well as rapid capacity attenuation.

All problems mentioned above will limit the further development of MXene-based materials for applications in sodium-ion batteries. Therefore, in future research, further optimization, exploration, and the development of new methods and new structures are required so that MXenes can have greater application prospects in SIBs. First, for the preparation of MXenes and MXene-based composites, it was necessary to explore F-free strategies with scaled-up production, such as the Lewis acid-related molten salt method. It is undoubtedly an important way to solve the problem where the current MXene synthesis method contains F, which is not environmentally friendly and has a high energy consumption rate due to it searching for a suitable etchant to obtain a better etching effect at a lower temperature. Furthermore, we are more inclined to develop new etching and stripping technologies, such as electrochemically assisted etching stripping or accurate interlayer atom removal assisted by multifield coupling. Second, it is also important to improve stability and avoid oxygen attacks on MXene-based materials. MXenes and some MXene-based composites are sensitive to oxygen. In general, in the wet chemical etching strategy, there is a large number of O terminations on MXene surfaces, which can reduce the active component due to byproduct generation. An important factor is to reduce the O terminations or replace them with other terminations, such as F/Cl/Br, even as the negatively charged organic molecules or polar molecules with an effective and controllable strategy. Third, the high charge voltage of MXene-based materials must be reduced. In aprotic SIB systems, the high charge voltage can significantly decrease the energy density of the full cell by about 20–30%. The new structure of the MXene substrate and the novel active component could be designed with Na⁺ desodiation kinetics and a lower desodiation energy barrier, which need a new structure or a useful, modified strategy to address the feedback of the as-prepared materials. It may also be necessary to use the effective assistance of DFT or other effective simulation technologies, or even a combination of material genomes and machine learning. Fourth, battery performance, especially lower coulombic efficiency and rapid capacity attenuation, should be improved. Coulombic efficiency needs to be improved to avoid the formation of dead sodium. MXene-based materials with highly reversible Na⁺ storage performance need to be employed, and SEI film could be further optimized with the effective addition. Long-term durability with lower capacity attenuation could also be promoted if we employed highly reversible Na⁺ storage structures and electrochemical stability. The most important thing to investigate is the structure–activity relationships between MXene compositions, morphologies, structures, surface functional groups, composites, and material properties, which are the bases of high-performance structural construction. For example, aiming at the problems of a high charging voltage, low specific capacities, and low capacity retention, the material structure could be adjusted in a targeted way to introduce active units such as sulfide and selenide, and MXene structures could be optimized to effectively suppress the shuttle effect. Finally, the sodium storage mechanism of MXene-based materials will be the focus in the future, and targeted feedback research based on the research mechanism may be more effective. With the research that is developing, MXene-based materials will present great advantages and application prospects in sodium-ion batteries and other related energy storage fields.

Author Contributions: Conceptualization, M.Y. and G.S.; methodology, Q.N. and Z.S.; investigation, M.Y., X.Z. and Z.C.; resources, J.X. and X.Z.; data curation, L.L. (Liu Lin) and L.L. (Luoqi Luo); writing—original draft preparation, M.Y. and J.X.; writing—review and editing, X.Z. and G.S.; funding acquisition, M.Y., G.S., and Z.S., M.Y. and X.Z. contributed equally to this work. The paper was prepared using all the authors' contributions. All authors have read and agreed to the published version of the manuscript.

Funding: This project was supported by the National Natural Science Foundation of China (22271018), the Talent Introduction and Scientific Research Funds of Beijing Normal University, the Youth Talent Promotion Project of the Beijing Association for Science and Technology, and the Interdisciplinary Fund of Beijing Normal University (BNUXKJC2216).

Data Availability Statement: Not applicable.

Conflicts of Interest: The authors declare no conflict of interest.

References

1. Ma, P.; Fang, D.; Liu, Y.; Shang, Y.; Shi, Y.; Yang, H.Y. MXene-Based Materials for Electrochemical Sodium-Ion Storage. *Adv. Sci.* **2021**, *8*, e2003185. [[CrossRef](#)]
2. Ni, Q.; Bai, Y.; Wu, F.; Wu, C. Polyanion-Type Electrode Materials for Sodium-Ion Batteries. *Adv. Sci.* **2017**, *4*, 1600275. [[CrossRef](#)]
3. Ansari, M.Z.; Seo, K.M.; Kim, S.H.; Ansari, S.A. Critical Aspects of Various Techniques for Synthesizing Metal Oxides and Fabricating Their Composite-Based Supercapacitor Electrodes: A Review. *Nanomaterials* **2022**, *12*, 1873. [[CrossRef](#)]
4. Wang, W.; Zhang, J.; Li, C.; Kou, X.; Li, B.; Yu, D.Y.W. P2-Na_{2/3}Ni_{2/3}Te_{1/3}O₂ Cathode for Na-ion Batteries with High Voltage and Excellent Stability. *Energy Environ. Mater.* **2022**. [[CrossRef](#)]
5. Liu, D.; Lu, S.; Xue, Y.; Guan, Z.; Fang, J.; Zhu, W.; Zhuang, Z. One-pot synthesis of IrNi@Ir core-shell nanoparticles as highly active hydrogen oxidation reaction electrocatalyst in alkaline electrolyte. *Nano Energy* **2019**, *59*, 26–32. [[CrossRef](#)]
6. Liu, B.; Sun, Y.; Liu, L.; Chen, J.; Yang, B.; Xu, S.; Yan, X. Recent advances in understanding Li–CO₂ electrochemistry. *Energy Environ. Sci.* **2019**, *12*, 887–922. [[CrossRef](#)]
7. Liu, B.; Chen, J.; Yang, B.; Liu, L.; Sun, Y.; Hou, R.; Lin, Z.; Yan, X. Boosting the performance of lithium metal capacitors with a Li composite anode. *J. Mater. Chem. A* **2021**, *9*, 10722–10730. [[CrossRef](#)]
8. Zhao, D.; Qin, J.; Zheng, L.; Cao, M. Amorphous Vanadium Oxide/Molybdenum Oxide Hybrid with Three-Dimensional Ordered Hierarchically Porous Structure as a High-Performance Li-Ion Battery Anode. *Chem. Mater.* **2016**, *28*, 4180–4190. [[CrossRef](#)]
9. Tran, M.-K.; DaCosta, A.; Mevawalla, A.; Panchal, S.; Fowler, M. Comparative Study of Equivalent Circuit Models Performance in Four Common Lithium-Ion Batteries: LFP, NMC, LMO, NCA. *Batteries* **2021**, *7*, 51. [[CrossRef](#)]
10. Kuntz, P.; Raccurt, O.; Azais, P.; Richter, K.; Waldmann, T.; Wohlfahrt-Mehrens, M.; Bardet, M.; Buzlukov, A.; Genies, S. Identification of Degradation Mechanisms by Post-Mortem Analysis for High Power and High Energy Commercial Li-Ion Cells after Electric Vehicle Aging. *Batteries* **2021**, *7*, 48. [[CrossRef](#)]
11. Zhang, S.; Liu, Y.; Hao, J.; Wallace, G.G.; Beirne, S.; Chen, J. 3D-Printed Wearable Electrochemical Energy Devices. *Adv. Funct. Mater.* **2021**, *32*, 2103092. [[CrossRef](#)]
12. He, X.-X.; Zhao, J.-H.; Lai, W.-H.; Yang, Z.; Gao, Y.; Zhang, H.; Qiao, Y.; Li, L.; Chou, S.-L. Challenges and Applications of Flexible Sodium Ion Batteries. *Mater. Lab* **2022**, *1*, 210001-1.
13. Wu, X.; Ru, Y.; Bai, Y.; Zhang, G.; Shi, Y.; Pang, H. PBA composites and their derivatives in energy and environmental applications. *Coord. Chem. Rev.* **2022**, *451*, 214260. [[CrossRef](#)]
14. Wang, N.; Chu, C.; Xu, X.; Du, Y.; Yang, J.; Bai, Z.; Dou, S. Comprehensive New Insights and Perspectives into Ti-Based Anodes for Next-Generation Alkaline Metal (Na⁺, K⁺) Ion Batteries. *Adv. Energy Mater.* **2018**, *8*, 1801888. [[CrossRef](#)]
15. Wang, F.; Liu, X.; Chen, L.; Chen, C.; Liu, Y.; Fan, L. Recent progress in key materials for room-temperature sodium-ion battery. *J. Electrochem.* **2019**, *25*, 55–76.
16. Chen, J.; Zhong, X.; He, C.; Wang, X.; Xu, Q.; Li, J. Synthesis and Raman Study of Hollow Core-Shell Ni_{1.2}Co_{0.8}P@N-C as an Anode Material for Sodium-Ion Batteries. *J. Electrochem.* **2020**, *26*, 328–337.
17. Kubota, K.; Dahbi, M.; Hosaka, T.; Kumakura, S.; Komaba, S. Towards K-Ion and Na-Ion Batteries as “Beyond Li-Ion”. *Chem. Rec.* **2018**, *18*, 459–479. [[CrossRef](#)]
18. Mu, L.-Q.; Hu, Y.-S.; Chen, L.-Q. New layered metal oxides as positive electrode materials for room-temperature sodium-ion batteries. *Chin. Phys. B* **2015**, *24*, 038202. [[CrossRef](#)]
19. Xu, X.; Liu, J.; Liu, J.; Ouyang, L.; Hu, R.; Wang, H.; Yang, L.; Zhu, M. A General Metal-Organic Framework (MOF)-Derived Selenidation Strategy for In Situ Carbon-Encapsulated Metal Selenides as High-Rate Anodes for Na-Ion Batteries. *Adv. Funct. Mater.* **2018**, *28*, 1707573. [[CrossRef](#)]
20. Wei, X.; Li, Y.; Peng, H.; Zhou, M.; Ou, Y.; Yang, Y.; Zhang, Y.; Xiao, P. Metal-organic framework-derived hollow CoS nanobox for high performance electrochemical energy storage. *Chem. Eng. J.* **2018**, *341*, 618–627. [[CrossRef](#)]
21. Zhao, C.; Lu, Y.; Chen, L.; Hu, Y.-S. Ni-based cathode materials for Na-ion batteries. *Nano Res.* **2019**, *12*, 2018–2030. [[CrossRef](#)]

22. Mohsin, I.U.; Ziebert, C.; Rohde, M.; Seifert, H.J. Thermophysical Characterization of a Layered P2 Type Structure $\text{Na}_{0.53}\text{MnO}_2$ Cathode Material for Sodium Ion Batteries. *Batteries* **2021**, *7*, 16. [[CrossRef](#)]
23. Nisa, S.S.; Rahmawati, M.; Yudha, C.S.; Nilasary, H.; Nursukatmo, H.; Oktaviano, H.S.; Muzayanha, S.U.; Purwanto, A. A Fast Approach to Obtain Layered Transition-Metal Cathode Material for Rechargeable Batteries. *Batteries* **2022**, *8*, 4. [[CrossRef](#)]
24. Zhang, T.; Zhang, L.; Hou, Y. MXenes: Synthesis strategies and lithium-sulfur battery applications. *eScience* **2022**, *2*, 164–182. [[CrossRef](#)]
25. Kajiyama, S.; Szabova, L.; Sodeyama, K.; Iinuma, H.; Morita, R.; Gotoh, K.; Tateyama, Y.; Okubo, M.; Yamada, A. Sodium-Ion Intercalation Mechanism in MXene Nanosheets. *ACS Nano* **2016**, *10*, 3334–3341. [[CrossRef](#)]
26. Aslam, M.K.; Xu, M. A Mini-Review: MXene composites for sodium/potassium-ion batteries. *Nanoscale* **2020**, *12*, 15993–16007. [[CrossRef](#)] [[PubMed](#)]
27. VahidMohammadi, A.; Rosen, J.; Gogotsi, Y. The world of two-dimensional carbides and nitrides (MXenes). *Science* **2021**, *372*, eabf1581. [[CrossRef](#)]
28. Li, M.; Mullaliu, A.; Passerini, S.; Giorgetti, M. Titanium Activation in Prussian Blue Based Electrodes for Na-ion Batteries: A Synthesis and Electrochemical Study. *Batteries* **2021**, *7*, 5. [[CrossRef](#)]
29. Mateen, A.; Ansari, M.Z.; Abbas, Q.; Muneeb, A.; Hussain, A.; Eldin, E.T.; Alzahrani, F.M.; Alsaiani, N.S.; Ali, S.; Javed, M.S. In Situ Nitrogen Functionalization of 2D- $\text{Ti}_3\text{C}_2\text{T}_x$ -MXenes for High-Performance Zn-Ion Supercapacitor. *Molecules* **2022**, *27*, 7446. [[CrossRef](#)]
30. Cao, Z.-J.; Zhang, Y.-Z.; Cui, Y.-L.-S.; Li, B.; Yang, S.-B. Harnessing the unique features of MXenes for sulfur cathodes. *Tungsten* **2020**, *2*, 162–175. [[CrossRef](#)]
31. Zheng, X.; Yuan, M.; Guo, D.; Wen, C.; Li, X.; Huang, X.; Li, H.; Sun, G. Theoretical Design and Structural Modulation of a Surface-Functionalized $\text{Ti}_3\text{C}_2\text{T}_x$ MXene-Based Heterojunction Electrocatalyst for a Li-Oxygen Battery. *ACS Nano* **2022**, *16*, 4487–4499. [[CrossRef](#)]
32. Aslam, M.K.; AlGarni, T.S.; Javed, M.S.; Shah, S.S.A.; Hussain, S.; Xu, M. 2D MXene Materials for Sodium Ion Batteries: A review on Energy Storage. *J. Energy Storage* **2021**, *37*, 102478. [[CrossRef](#)]
33. Meng, J.; Zhang, F.; Zhang, L.; Liu, L.; Chen, J.; Yang, B.; Yan, X. Rolling up MXene sheets into scrolls to promote their anode performance in lithium-ion batteries. *J. Energy Chem.* **2020**, *46*, 256–263. [[CrossRef](#)]
34. Wen, C.; Zheng, X.; Li, X.; Yuan, M.; Li, H.; Sun, G. Rational design of 3D hierarchical MXene@ AlF_3 / $\text{Ni}(\text{OH})_2$ nanohybrid for high-performance lithium-sulfur batteries. *Chem. Eng. J.* **2021**, *409*, 128102. [[CrossRef](#)]
35. Hussain, I.; Lamiel, C.; Sahoo, S.; Ahmad, M.; Chen, X.; Javed, M.S.; Qin, N.; Gu, S.; Li, Y.; Nawaz, T.; et al. Factors affecting the growth formation of nanostructures and their impact on electrode materials: A systematic review. *Mater. Today Phys.* **2022**, *27*, 100844. [[CrossRef](#)]
36. Hussain, I.; Lamiel, C.; Sufyan Javed, M.; Ahmad, M.; Chen, X.; Sahoo, S.; Ma, X.; Bajaber, M.A.; Zahid Ansari, M.; Zhang, K. Earth- and marine-life-resembling nanostructures for electrochemical energy storage. *Chem. Eng. J.* **2023**, *454*, 140313. [[CrossRef](#)]
37. Xie, X.; Kretschmer, K.; Anasori, B.; Sun, B.; Wang, G.; Gogotsi, Y. Porous $\text{Ti}_3\text{C}_2\text{T}_x$ MXene for Ultrahigh-Rate Sodium-Ion Storage with Long Cycle Life. *ACS Appl. Nano Mater.* **2018**, *1*, 505–511. [[CrossRef](#)]
38. Li, H.; Liu, A.; Ren, X.; Yang, Y.; Gao, L.; Fan, M.; Ma, T. A black phosphorus/ Ti_3C_2 MXene nanocomposite for sodium-ion batteries: A combined experimental and theoretical study. *Nanoscale* **2019**, *11*, 19862–19869. [[CrossRef](#)]
39. Tahir, M.; Khan, A.A.; Tasleem, S.; Mansoor, R.; Sherryna, A.; Tahir, B. Recent advances in titanium carbide MXene-based nanotextures with influential effect of synthesis parameters for solar CO_2 reduction and H_2 production: A critical review. *J. Energy Chem.* **2023**, *76*, 295–331. [[CrossRef](#)]
40. Salim, O.; Mahmoud, K.A.; Pant, K.K.; Joshi, R.K. Introduction to MXenes: Synthesis and characteristics. *Mater. Today Chem.* **2019**, *14*, 100191. [[CrossRef](#)]
41. Hong, L.-F.; Guo, R.-T.; Yuan, Y.; Ji, X.-Y.; Li, Z.-S.; Lin, Z.-D.; Pan, W.-G. Recent progress of two-dimensional MXenes in photocatalytic applications: A review. *Mater. Today Energy* **2020**, *18*, 100521. [[CrossRef](#)]
42. Yuan, Z.; Wang, L.; Li, D.; Cao, J.; Han, W. Carbon-Reinforced Nb_2CT_x MXene/ MoS_2 Nanosheets as a Superior Rate and High-Capacity Anode for Sodium-Ion Batteries. *ACS Nano* **2021**, *15*, 7439–7450. [[CrossRef](#)] [[PubMed](#)]
43. Shuck, C.E.; Sarycheva, A.; Anayee, M.; Levitt, A.; Zhu, Y.; Uzun, S.; Balitskiy, V.; Zahorodna, V.; Gogotsi, O.; Gogotsi, Y. Scalable Synthesis of $\text{Ti}_3\text{C}_2\text{T}_x$ MXene. *Adv. Eng. Mater.* **2020**, *22*, 1901241. [[CrossRef](#)]
44. Ibragimova, R.; Puska, M.J.; Komsa, H.P. pH-Dependent Distribution of Functional Groups on Titanium-Based MXenes. *ACS Nano* **2019**, *13*, 9171–9181. [[CrossRef](#)] [[PubMed](#)]
45. Mashtalir, O.; Naguib, M.; Mochalin, V.N.; Dall’Agnese, Y.; Heon, M.; Barsoum, M.W.; Gogotsi, Y. Intercalation and delamination of layered carbides and carbonitrides. *Nat. Commun.* **2013**, *4*, 1716. [[CrossRef](#)] [[PubMed](#)]
46. Lipatov, A.; Alhabeab, M.; Lukatskaya, M.R.; Boson, A.; Gogotsi, Y.; Sinitskii, A. Effect of Synthesis on Quality, Electronic Properties and Environmental Stability of Individual Monolayer Ti_3C_2 MXene Flakes. *Adv. Electron. Mater.* **2016**, *2*, 1600255. [[CrossRef](#)]
47. Jawaid, A.; Hassan, A.; Neher, G.; Nepal, D.; Pachter, R.; Kennedy, W.J.; Ramakrishnan, S.; Vaia, R.A. Halogen Etch of Ti_3AlC_2 MAX Phase for MXene Fabrication. *ACS Nano* **2021**, *15*, 2771–2777. [[CrossRef](#)]
48. Shi, H.; Zhang, P.; Liu, Z.; Park, S.; Lohe, M.R.; Wu, Y.; Shaygan Nia, A.; Yang, S.; Feng, X. Ambient-Stable Two-Dimensional Titanium Carbide (MXene) Enabled by Iodine Etching. *Angew. Chem. Int. Ed.* **2021**, *60*, 8689–8693. [[CrossRef](#)]

49. Sun, Z.; Yuan, M.; Lin, L.; Yang, H.; Nan, C.; Li, H.; Sun, G.; Yang, X. Selective Lithiation–Expansion–Microexplosion Synthesis of Two-Dimensional Fluoride-Free MXene. *ACS Mater. Lett.* **2019**, *1*, 628–632. [[CrossRef](#)]
50. Han, Q.; Zhou, Y.; Du, R.; Xiao, B.; Cheng, J.; Zhang, M.; Dong, C.; Sun, X.; Jiang, F.; Yang, J. $\text{Ti}_3\text{C}_2\text{T}_x$ with a hydroxyl-rich surface for metal sulfides as high performance electrode materials for sodium/lithium storage. *J. Mater. Chem. A* **2021**, *9*, 14013–14024. [[CrossRef](#)]
51. Wyatt, B.C.; Nemani, S.K.; Anasori, B. 2D transition metal carbides (MXenes) in metal and ceramic matrix composites. *Nano Con.* **2021**, *8*, 16. [[CrossRef](#)] [[PubMed](#)]
52. Gou, L.; Jing, W.; Li, Y.; Wang, M.; Hu, S.; Wang, H.; He, Y.-B. Lattice-Coupled Si/MXene Confined by Hard Carbon for Fast Sodium-Ion Conduction. *ACS Appl. Energy Mater.* **2021**, *4*, 7268–7277. [[CrossRef](#)]
53. Zhang, W.; Pan, Z.-Z.; Lv, W.; Lv, R.; Shen, W.; Kang, F.; Yang, Q.-H.; Weng, Y.; Huang, Z.-H. Wasp nest-imitated assembly of elastic rGO/p- $\text{Ti}_3\text{C}_2\text{T}_x$ MXene-cellulose nanofibers for high-performance sodium-ion batteries. *Carbon* **2019**, *153*, 625–633. [[CrossRef](#)]
54. Zhang, S.; Li, X.Y.; Yang, W.; Tian, H.; Han, Z.; Ying, H.; Wang, G.; Han, W.Q. Novel Synthesis of Red Phosphorus Nanodot/ $\text{Ti}_3\text{C}_2\text{T}_x$ MXenes from Low-Cost Ti_3SiC_2 MAX Phases for Superior Lithium- and Sodium-Ion Batteries. *ACS Appl. Mater. Interfaces* **2019**, *11*, 42086–42093. [[CrossRef](#)] [[PubMed](#)]
55. Meng, R.; Huang, J.; Feng, Y.; Zu, L.; Peng, C.; Zheng, L.; Zheng, L.; Chen, Z.; Liu, G.; Chen, B.; et al. Black Phosphorus Quantum Dot/ Ti_3C_2 MXene Nanosheet Composites for Efficient Electrochemical Lithium/Sodium-Ion Storage. *Adv. Energy Mater.* **2018**, *8*, 1801514. [[CrossRef](#)]
56. Yang, E.; Ji, H.; Kim, J.; Kim, H.; Jung, Y. Exploring the possibilities of two-dimensional transition metal carbides as anode materials for sodium batteries. *Phys. Chem. Chem. Phys.* **2015**, *17*, 5000–5005. [[CrossRef](#)] [[PubMed](#)]
57. Lv, G.; Wang, J.; Shi, Z.; Fan, L. Intercalation and delamination of two-dimensional MXene ($\text{Ti}_3\text{C}_2\text{T}_x$) and application in sodium-ion batteries. *Mater. Lett.* **2018**, *219*, 45–50. [[CrossRef](#)]
58. Liang, K.; Tabassum, A.; Majed, A.; Dun, C.; Yang, F.; Guo, J.; Prenger, K.; Urban, J.J.; Naguib, M. Synthesis of new two-dimensional titanium carbonitride $\text{Ti}_2\text{C}_{0.5}\text{N}_{0.5}\text{T}_x$ MXene and its performance as an electrode material for sodium-ion battery. *InfoMat* **2021**, *3*, 1422–1430. [[CrossRef](#)]
59. Du, L.; Duan, H.; Xia, Q.; Jiang, C.; Yan, Y.; Wu, S. Hybrid Charge-Storage Route to Nb_2CT_x MXene as Anode for Sodium-Ion Batteries. *ChemistrySelect* **2020**, *5*, 1186–1192. [[CrossRef](#)]
60. Zhao, M.Q.; Xie, X.; Ren, C.E.; Makaryan, T.; Anasori, B.; Wang, G.; Gogotsi, Y. Hollow MXene Spheres and 3D Macroporous MXene Frameworks for Na-Ion Storage. *Adv. Mater.* **2017**, *29*, 1702410. [[CrossRef](#)]
61. Ming, K.; Zhang, Z.; Li, H. Creating porous texture on $\text{Ti}_3\text{C}_2\text{T}_x$ for enhanced sodium-ion battery anode. *J. Mater. Sci.* **2022**, *57*, 14959–14968. [[CrossRef](#)]
62. Lian, P.; Dong, Y.; Wu, Z.-S.; Zheng, S.; Wang, X.; Sen, W.; Sun, C.; Qin, J.; Shi, X.; Bao, X. Alkalized Ti_3C_2 MXene nanoribbons with expanded interlayer spacing for high-capacity sodium and potassium ion batteries. *Nano Energy* **2017**, *40*, 1–8. [[CrossRef](#)]
63. Song, X.; Wang, H.; Jin, S.; Lv, M.; Zhang, Y.; Kong, X.; Xu, H.; Ma, T.; Luo, X.; Tan, H.; et al. Oligolayered $\text{Ti}_3\text{C}_2\text{T}_x$ MXene towards high performance lithium/sodium storage. *Nano Res.* **2020**, *13*, 1659–1667. [[CrossRef](#)]
64. Zhao, D.; Clites, M.; Ying, G.; Kota, S.; Wang, J.; Natu, V.; Wang, X.; Pomerantseva, E.; Cao, M.; Barsoum, M.W. Alkali-induced crumpling of $\text{Ti}_3\text{C}_2\text{T}_x$ (MXene) to form 3D porous networks for sodium ion storage. *Chem. Commun.* **2018**, *54*, 4533–4536. [[CrossRef](#)] [[PubMed](#)]
65. Luo, J.; Fang, C.; Jin, C.; Yuan, H.; Sheng, O.; Fang, R.; Zhang, W.; Huang, H.; Gan, Y.; Xia, Y.; et al. Tunable pseudocapacitance storage of MXene by cation pillaring for high performance sodium-ion capacitors. *J. Mater. Chem. A* **2018**, *6*, 7794–7806. [[CrossRef](#)]
66. Li, J.; Yan, D.; Hou, S.; Li, Y.; Lu, T.; Yao, Y.; Pan, L. Improved sodium-ion storage performance of $\text{Ti}_3\text{C}_2\text{T}_x$ MXenes by sulfur doping. *J. Mater. Chem. A* **2018**, *6*, 1234–1243. [[CrossRef](#)]
67. Sun, S.; Xie, Z.; Yan, Y.; Wu, S. Hybrid energy storage mechanisms for sulfur-decorated Ti_3C_2 MXene anode material for high-rate and long-life sodium-ion batteries. *Chem. Eng. J.* **2019**, *366*, 460–467. [[CrossRef](#)]
68. Natu, V.; Clites, M.; Pomerantseva, E.; Barsoum, M.W. Mesoporous MXene powders synthesized by acid induced crumpling and their use as Na-ion battery anodes. *Mater. Res. Lett.* **2018**, *6*, 230–235. [[CrossRef](#)]
69. Sun, N.; Zhu, Q.; Anasori, B.; Zhang, P.; Liu, H.; Gogotsi, Y.; Xu, B. MXene-Bonded Flexible Hard Carbon Film as Anode for Stable Na/K-Ion Storage. *Adv. Funct. Mater.* **2019**, *29*, 1906282. [[CrossRef](#)]
70. Zhang, P.; Soomro, R.A.; Guan, Z.; Sun, N.; Xu, B. 3D carbon-coated MXene architectures with high and ultrafast lithium/sodium-ion storage. *Energy Storage Mater.* **2020**, *29*, 163–171. [[CrossRef](#)]
71. Wei, C.; Cao, H.; Deng, W.; Zhao, M.; Guo, C.; Liu, P.; Xu, B.; Guo, J. Graphene-mediated dense integration of $\text{Ti}_3\text{C}_2\text{T}_x$ MXene monoliths for compact energy storage: Balancing kinetics and packing density. *Appl. Surf. Sci.* **2022**, *604*, 154565. [[CrossRef](#)]
72. Wang, H.-Q.; Zhao, Y.-X.; Gou, L.; Wang, L.-Y.; Wang, M.; Li, Y.; Hu, S.-L. Rational construction of densely packed Si/MXene composite microspheres enables favorable sodium storage. *Rare Metals* **2022**, *41*, 1626–1636. [[CrossRef](#)]
73. Zhao, R.; Qian, Z.; Liu, Z.; Zhao, D.; Hui, X.; Jiang, G.; Wang, C.; Yin, L. Molecular-level heterostructures assembled from layered black phosphorene and Ti_3C_2 MXene as superior anodes for high-performance sodium ion batteries. *Nano Energy* **2019**, *65*, 104037. [[CrossRef](#)]

74. Jin, X.; Zhang, W.; Liu, S.; Zhang, T.; Song, Z.; Shao, W.; Mao, R.; Yao, M.; Jian, X.; Hu, F. Highly stable $\text{Ti}_3\text{C}_2\text{T}_x$ MXene-based sandwich-like structure via interfacial self-assembly of nitrogen-rich polymer network for superior sodium-ion storage performance. *Chem. Eng. J.* **2023**, *451*, 138763. [[CrossRef](#)]
75. Wang, X.; Wang, J.; Qin, J.; Xie, X.; Yang, R.; Cao, M. Surface Charge Engineering for Covalently Assembling Three-Dimensional MXene Network for All-Climate Sodium Ion Batteries. *ACS Appl. Mater. Interfaces* **2020**, *12*, 39181–39194. [[CrossRef](#)]
76. Huang, J.; Meng, R.; Zu, L.; Wang, Z.; Feng, N.; Yang, Z.; Yu, Y.; Yang, J. Sandwich-like $\text{Na}_{0.23}\text{TiO}_2$ nanobelt/ Ti_3C_2 MXene composites from a scalable in situ transformation reaction for long-life high-rate lithium/sodium-ion batteries. *Nano Energy* **2018**, *46*, 20–28. [[CrossRef](#)]
77. Guo, X.; Zhang, J.; Song, J.; Wu, W.; Liu, H.; Wang, G. MXene encapsulated titanium oxide nanospheres for ultra-stable and fast sodium storage. *Energy Storage Mater.* **2018**, *14*, 306–313. [[CrossRef](#)]
78. Wang, F.; Ma, X.; Zou, P.; Wang, G.; Xiong, Y.; Liu, Y.; Ren, F.; Xiong, X. Nitrogen-doped carbon decorated $\text{TiO}_2/\text{Ti}_3\text{C}_2\text{T}_x$ MXene composites as anode material for high-performance sodium-ion batteries. *Surf. Coat. Technol.* **2021**, *422*, 127568. [[CrossRef](#)]
79. Yang, C.; Liu, Y.; Sun, X.; Zhang, Y.; Hou, L.; Zhang, Q.; Yuan, C. In-situ construction of hierarchical accordion-like $\text{TiO}_2/\text{Ti}_3\text{C}_2$ nanohybrid as anode material for lithium and sodium ion batteries. *Electrochim. Acta* **2018**, *271*, 165–172. [[CrossRef](#)]
80. Wang, P.; Lu, X.; Boyjoo, Y.; Wei, X.; Zhang, Y.; Guo, D.; Sun, S.; Liu, J. Pillar-free $\text{TiO}_2/\text{Ti}_3\text{C}_2$ composite with expanded interlayer spacing for high-capacity sodium ion batteries. *J. Power Sources* **2020**, *451*, 227756. [[CrossRef](#)]
81. Gao, P.; Shi, H.; Ma, T.; Liang, S.; Xia, Y.; Xu, Z.; Wang, S.; Min, C.; Liu, L. MXene/ TiO_2 Heterostructure-Decorated Hard Carbon with Stable Ti-O-C Bonding for Enhanced Sodium-Ion Storage. *ACS Appl. Mater. Interfaces* **2021**, *13*, 51028–51038. [[CrossRef](#)] [[PubMed](#)]
82. Guo, X.; Xie, X.; Choi, S.; Zhao, Y.; Liu, H.; Wang, C.; Chang, S.; Wang, G. $\text{Sb}_2\text{O}_3/\text{MXene}(\text{Ti}_3\text{C}_2\text{T}_x)$ hybrid anode materials with enhanced performance for sodium-ion batteries. *J. Mater. Chem. A* **2017**, *5*, 12445–12452. [[CrossRef](#)]
83. Tao, M.; Zhang, Y.; Zhan, R.; Guo, B.; Xu, Q.; Xu, M. A chemically bonded CoNiO_2 nanoparticles/MXene composite as anode for sodium-ion batteries. *Mater. Lett.* **2018**, *230*, 173–176. [[CrossRef](#)]
84. Chen, Y.; Sun, Y.; Geng, M.; Shao, W.; Chen, Y.; Liu, X.; Ou, M. $\text{SnO}_2/\text{MXene}$ nanoparticles as a superior high-rate and cycling-stable anode for sodium ion batteries. *Mater. Lett.* **2021**, *304*, 130704. [[CrossRef](#)]
85. Wu, F.; Jiang, Y.; Ye, Z.; Huang, Y.; Wang, Z.; Li, S.; Mei, Y.; Xie, M.; Li, L.; Chen, R. A 3D flower-like VO_2/MXene hybrid architecture with superior anode performance for sodium ion batteries. *J. Mater. Chem. A* **2019**, *7*, 1315–1322. [[CrossRef](#)]
86. Du, G.; Tao, M.; Gao, W.; Zhang, Y.; Zhan, R.; Bao, S.; Xu, M. Preparation of $\text{MoS}_2/\text{Ti}_3\text{C}_2\text{T}_x$ composite as anode material with enhanced sodium/lithium storage performance. *Inorg. Chem. Front.* **2019**, *6*, 117–125. [[CrossRef](#)]
87. Zhang, X.; Shi, H.; Liu, L.; Min, C.; Liang, S.; Xu, Z.; Xue, Y.; Hong, C.; Cai, Z. Construction of $\text{MoS}_2/\text{MXene}$ heterostructure on stress-modulated kapok fiber for high-rate sodium-ion batteries. *J. Colloid Interf. Sci.* **2022**, *605*, 472–482. [[CrossRef](#)] [[PubMed](#)]
88. Yuan, Z.; Cao, J.; Valerii, S.; Xu, H.; Wang, L.; Han, W. MXene-Bonded hollow $\text{MoS}_2/\text{Carbon}$ sphere strategy for high-performance flexible sodium ion storage. *Chem. Eng. J.* **2022**, *430*, 132755. [[CrossRef](#)]
89. Huang, P.; Ying, H.; Zhang, S.; Zhang, Z.; Han, W.Q. Molten Salts Etching Route Driven Universal Construction of MXene/Transition Metal Sulfides Heterostructures with Interfacial Electronic Coupling for Superior Sodium Storage. *Adv. Energy Mater.* **2022**, *12*, 2202052. [[CrossRef](#)]
90. Wu, Y.; Nie, P.; Wu, L.; Dou, H.; Zhang, X. 2D MXene/ SnS_2 composites as high-performance anodes for sodium ion batteries. *Chem. Eng. J.* **2018**, *334*, 932–938. [[CrossRef](#)]
91. Zang, R.; Li, P.; Wang, G. Bimetallic Sulfide/Sulfur Doped $\text{T}_3\text{C}_2\text{T}_x$ MXene Nanocomposites as High-performance Anode Materials for Sodium-ion Batteries. *Chem. Res. Univ.* **2020**, *36*, 431–438. [[CrossRef](#)]
92. Zhang, Y.; Zhan, R.; Xu, Q.; Liu, H.; Tao, M.; Luo, Y.; Bao, S.; Li, C.; Xu, M. Circuit board-like CoS/MXene composite with superior performance for sodium storage. *Chem. Eng. J.* **2019**, *357*, 220–225. [[CrossRef](#)]
93. Huang, P.; Ying, H.; Zhang, S.; Zhang, Z.; Han, W.-Q. In situ fabrication of MXene/ CuS hybrids with interfacial covalent bonding via Lewis acidic etching route for efficient sodium storage. *J. Mater. Chem. A* **2022**, *10*, 22135–22144. [[CrossRef](#)]
94. Zhang, Y.; Guo, B.; Hu, L.; Xu, Q.; Li, Y.; Liu, D.; Xu, M. Synthesis of SnS nanoparticle-modified MXene ($\text{Ti}_3\text{C}_2\text{T}_x$) composites for enhanced sodium storage. *J. Alloy. Compd.* **2018**, *732*, 448–453. [[CrossRef](#)]
95. Zhang, H.; Ren, M.; Jiang, W.; Yao, J.; Pan, L.; Yang, J. Hierarchical $\text{Sb}_2\text{S}_3@m\text{-Ti}_3\text{C}_2\text{T}_x$ composite anode with enhanced Na-ion storage properties. *J. Alloy. Compd.* **2021**, *887*, 161318. [[CrossRef](#)]
96. Xie, X.; Makaryan, T.; Zhao, M.; Van Aken, K.L.; Gogotsi, Y.; Wang, G. MoS_2 Nanosheets Vertically Aligned on Carbon Paper: A Freestanding Electrode for Highly Reversible Sodium-Ion Batteries. *Adv. Energy Mater.* **2016**, *6*, 1502161. [[CrossRef](#)]
97. Wu, Y.; Nie, P.; Jiang, J.; Ding, B.; Dou, H.; Zhang, X. MoS_2 -Nanosheet-Decorated 2D Titanium Carbide (MXene) as High-Performance Anodes for Sodium-Ion Batteries. *ChemElectroChem* **2017**, *4*, 1560–1565. [[CrossRef](#)]
98. He, F.; Tang, C.; Liu, Y.; Li, H.; Du, A.; Zhang, H. Carbon-coated MoS_2 nanosheets@CNTs- Ti_3C_2 MXene quaternary composite with the superior rate performance for sodium-ion batteries. *J. Mater. Sci. Technol.* **2022**, *100*, 101–109. [[CrossRef](#)]
99. Wen, B.; Kong, N.; Huang, M.; Fu, L.; Yan, D.; Tian, Y.; Liu, J.; Tan, R.; Han, F. 1T-2H $\text{MoS}_2/\text{Ti}_3\text{C}_2$ MXene Heterostructure with High-Rate and High-Capacity Performance for Sodium-Ion Batteries. *Energy & Fuels* **2022**, *36*, 11234–11244.
100. Zhang, H.; Song, J.; Li, J.; Feng, J.; Ma, Y.; Ma, L.; Liu, H.; Qin, Y.; Zhao, X.; Wang, F. Interlayer-Expanded MoS_2 Nanoflowers Vertically Aligned on MXene@Dual-Phased TiO_2 as High-Performance Anode for Sodium-Ion Batteries. *ACS Appl. Mater. Interfaces* **2022**, *14*, 16300–16309. [[CrossRef](#)]

101. Zhang, W.X.; Zhang, J.H.; Zhang, Y.K.; He, C.; Zhao, P. NiS₂ nanoparticles anchored on MXene conductive frameworks with enhanced lithium and sodium storage properties. *Ionics* **2022**, *28*, 4621–4629. [[CrossRef](#)]
102. Liu, X.; Wang, M.; Qin, B.; Zhang, Y.; Liu, Z.; Fan, H. 2D-2D MXene/ReS₂ hybrid from Ti₃C₂T_x MXene conductive layers supporting ultrathin ReS₂ nanosheets for superior sodium storage. *Chem. Eng. J.* **2022**, *431*, 133796. [[CrossRef](#)]
103. Yang, J.; Wang, T.; Guo, X.; Sheng, X.; Li, J.; Wang, C.; Wang, G. Flexible sodium-ion capacitors boosted by high electrochemically-reactive and structurally-stable Sb₂S₃ nanowire/Ti₃C₂T_x MXene film anodes. *Nano Res.* **2021**. [[CrossRef](#)]
104. Wang, H.; Song, X.; Lv, M.; Jin, S.; Xu, J.; Kong, X.; Li, X.; Liu, Z.; Chang, X.; Sun, W.; et al. Interfacial Covalent Bonding Endowing Ti₃C₂-Sb₂S₃ Composites High Sodium Storage Performance. *Small* **2022**, *18*, e2104293. [[CrossRef](#)] [[PubMed](#)]
105. Fan, T.; Wu, Y.; Li, J.; Zhong, W.; Tang, W.; Zhang, X.; Xu, M. Sheet-to-layer structure of SnSe₂/MXene composite materials for advanced sodium ion battery anodes. *New J. Chem.* **2021**, *45*, 1944–1952. [[CrossRef](#)]
106. Tan, Y.; Yi, M.; Zhu, Z.; Zhang, X.; Qin, K.; Zhang, J.; Rongshu, Z. Carbon-coated MoSe₂/MXene heterostructures as active materials for high-performance Na⁺ batteries. *Mater. Today Commun.* **2022**, *31*, 103740. [[CrossRef](#)]
107. Xu, E.; Li, P.; Quan, J.; Zhu, H.; Wang, L.; Chang, Y.; Sun, Z.; Chen, L.; Yu, D.; Jiang, Y. Dimensional Gradient Structure of CoSe₂@CNTs-MXene Anode Assisted by Ether for High-Capacity, Stable Sodium Storage. *Nano-micro Lett.* **2021**, *13*, 40. [[CrossRef](#)]
108. Deng, Q.; Wang, M.; Liu, X.; Fan, H.; Zhang, Y.; Yang, H.Y. Ultrathin cobalt nickel selenides (Co_{0.5}Ni_{0.5}Se₂) nanosheet arrays anchoring on Ti₃C₂ MXene for high-performance Na⁺/K⁺ batteries. *J. Colloid Interf. Sci.* **2022**, *626*, 700–709. [[CrossRef](#)]
109. Dong, Y.; Wu, Z.S.; Zheng, S.; Wang, X.; Qin, J.; Wang, S.; Shi, X.; Bao, X. Ti₃C₂ MXene-Derived Sodium/Potassium Titanate Nanoribbons for High-Performance Sodium/Potassium Ion Batteries with Enhanced Capacities. *ACS Nano* **2017**, *11*, 4792–4800. [[CrossRef](#)]
110. Fang, Y.; Zhang, Y.; Miao, C.; Zhu, K.; Chen, Y.; Du, F.; Yin, J.; Ye, K.; Cheng, K.; Yan, J.; et al. MXene-Derived Defect-Rich TiO₂@rGO as High-Rate Anodes for Full Na Ion Batteries and Capacitors. *Nano-micro Lett.* **2020**, *12*, 128. [[CrossRef](#)]
111. Tang, J.; Huang, X.; Lin, T.; Qiu, T.; Huang, H.; Zhu, X.; Gu, Q.; Luo, B.; Wang, L. MXene derived TiS₂ nanosheets for high-rate and long-life sodium-ion capacitors. *Energy Storage Mater.* **2020**, *26*, 550–559. [[CrossRef](#)]
112. Xiao, J.; Wu, B.; Bai, L.; Ma, X.; Lu, H.; Yao, J.; Zhang, C.; Gao, H. Ag Nanoparticles decorated few-layer Nb₂CT nanosheets architectures with superior lithium/sodium-ion storage. *Electrochim. Acta* **2022**, *402*, 139566. [[CrossRef](#)]
113. Liu, X.; Liu, F.; Zhao, X.; Fan, L.-Z. Constructing MOF-derived CoP-NC@MXene sandwich-like composite by in-situ intercalation for enhanced lithium and sodium storage. *J. Mater.* **2022**, *8*, 30–37. [[CrossRef](#)]
114. Yang, C.; Sun, X.; Zhang, Y.R.; Liu, Y.; Zhang, Q.A.; Yuan, C.Z. Facile synthesis of hierarchical NaTi₂(PO₄)₃/Ti₃C₂ nanocomposites with superior sodium storage performance. *Mater. Lett.* **2019**, *236*, 408–411. [[CrossRef](#)]
115. Zhang, S.; Ying, H.; Huang, P.; Wang, J.; Zhang, Z.; Zhang, Z.; Han, W.-Q. Ultrafine Sb Pillared Few-Layered Ti₃C₂T_x MXenes for Advanced Sodium Storage. *ACS Appl. Energy Mater.* **2021**, *4*, 9806–9815. [[CrossRef](#)]
116. Chen, H.; Chen, N.; Zhang, M.; Li, M.; Gao, Y.; Wang, C.; Chen, G.; Du, F. Ti₃C₂T_x MXene decorated with Sb nanoparticles as anodes material for sodium-ion batteries. *Nanotechnology* **2019**, *30*, 134001. [[CrossRef](#)]
117. Xu, H.; Fan, J.; Pang, D.; Zheng, Y.; Chen, G.; Du, F.; Gogotsi, Y.; Dall’Agnese, Y.; Gao, Y. Synergy of ferric vanadate and MXene for high performance Li- and Na-ion batteries. *Chem. Eng. J.* **2022**, *436*, 135012. [[CrossRef](#)]
118. Yang, Q.; Jiao, T.; Li, M.; Li, Y.; Ma, L.; Mo, F.; Liang, G.; Wang, D.; Wang, Z.; Ruan, Z.; et al. In situ formation of NaTi₂(PO₄)₃ cubes on Ti₃C₂ MXene for dual-mode sodium storage. *J. Mater. Chem. A* **2018**, *6*, 18525–18532. [[CrossRef](#)]
119. Ding, Y.; Chen, Y.; Xu, N.; Lian, X.; Li, L.; Hu, Y.; Peng, S. Facile Synthesis of FePS₃ Nanosheets@MXene Composite as a High-Performance Anode Material for Sodium Storage. *Nano-micro Lett.* **2020**, *12*, 54. [[CrossRef](#)]
120. Ma, H.; Li, J.; Yang, J.; Wang, N.; Liu, Z.; Wang, T.; Su, D.; Wang, C.; Wang, G. Bismuth Nanoparticles Anchored on Ti₃C₂T_x MXene Nanosheets for High-Performance Sodium-Ion Batteries. *Chem. Asian J.* **2021**, *16*, 3774–3780. [[CrossRef](#)]
121. Wang, H.; Wang, P.; Gan, W.; Ci, L.; Li, D.; Yuan, Q. VS₄ nanoarrays pillared Ti₃C₂T_x with enlarged interlayer spacing as anode for advanced lithium/sodium ion battery and hybrid capacitor. *J. Power Sources* **2022**, *534*, 231412. [[CrossRef](#)]
122. Zhong, W.; Tao, M.; Tang, W.; Gao, W.; Yang, T.; Zhang, Y.; Zhan, R.; Bao, S.-J.; Xu, M. MXene-derivative pompon-like Na₂Ti₃O₇@C anode material for advanced sodium ion batteries. *Chem. Eng. J.* **2019**, *378*, 122209. [[CrossRef](#)]

Disclaimer/Publisher’s Note: The statements, opinions and data contained in all publications are solely those of the individual author(s) and contributor(s) and not of MDPI and/or the editor(s). MDPI and/or the editor(s) disclaim responsibility for any injury to people or property resulting from any ideas, methods, instructions or products referred to in the content.